A High-order Accurate Scheme for Maxwell's Equations with a Generalized Dispersive Material Model

Jordan B. Angel[a,1,1,2], Jeffrey W. Banks[a,1,3], William D. Henshaw[a,1,*], Michael J. Jenkinson[a,1,4],
Alexander V. Kildishev[b,1], Gregor Kovačič[a,1,5], Ludmila Prokopeva[b,1],
Donald W. Schwendeman[a,1]

[a] *Department of Mathematical Sciences, Rensselaer Polytechnic Institute, Troy, NY 12180, USA*
[b] *School of Electrical and Computer Engineering, Purdue University, West Lafayette, IN 47907, USA*

Abstract

A high-order accurate scheme for solving the time-domain Maxwell's equations with a generalized dispersive material model is described. The equations for the electric field are solved in second-order form, and a general dispersion model is treated with the addition of one or more polarization vectors which obey a set of auxiliary differential equations (ADE). Numerical methods are developed for both second-order and fourth-order accuracy in space and time. The equations are discretized using finite-differences, and advanced in time with a single-stage, three-level, space-time scheme which remains stable up to the usual explicit CFL restriction, as proven using mode analysis. Because the equations are treated in their second-order form, there is no need for grid staggering, and instead a collocated grid is used. Composite overlapping grids are used to treat complex geometries with boundary-conforming grids, and a high-order upwind dissipation is added to ensure robust and stable approximations on overlapping grids. Numerical results in two and three space dimensions confirm the accuracy and stability of the new schemes.

Keywords: generalized dispersive material model; dispersive FDTD; electromagnetics; composite overlapping grids

---

Contents

---

[*] Corresponding author

Email addresses: `angelj2@rpi.edu` (Jordan B. Angel), `banksj3@rpi.edu` (Jeffrey W. Banks), `henshw@rpi.edu` (William D. Henshaw), `jenkim22@rpi.edu` (Michael J. Jenkinson), `kildishev@purdue.edu` (Alexander V. Kildishev), `kovacg@rpi.edu` (Gregor Kovačič), `lprokop@purdue.edu` (Ludmila Prokopeva), `schwed@rpi.edu` (Donald W. Schwendeman)

[1] This work was partially funded by the DARPA Defense Sciences Office, Award HR00111720032.
[2] This work was partially funded under DOD contract W911NF-14-C-0161.
[3] Research supported by a U.S. Presidential Early Career Award for Scientists and Engineers.
[4] This work was partially funded by the NSF Research Training Group Grant DMS-1344962.
[5] This work was partially funded by NSF Grant DMS-1615859.

1. Introduction

Maxwell's equations in the time-domain are usually solved in first-order form, and there is a wide class of methods available for their numerical solution. These include those based on finite difference, spectral, pseudo-spectral, finite-element, and discontinuous Galerkin methods, among others. The literature is very broad, and good overviews can be found in the review by Hestaven [1], or the references books by Taflove [2] and Cohen [3]. The first-order spatial formulation, however, has certain challenges, not the least of which is the fact that standard centered differences and continuous finite elements on collocated grids result in a discretization with a large unphysical null-space due to the discrete treatment of the curl operator. This difficulty can be overcome in the first-order formulation through the use of staggered grids for finite difference methods (e.g. the well-known Yee scheme [4]), or through the use of special edge elements (e.g. Nedelec finite elements [5]). The addition of dissipation to the collocated equations in first-order form can also be used as a remedy. The alternative approach taken here is to treat the equations in their second-order formulation. As discussed in [6, 7], this approach naturally leads to compact high-order accurate approximations of Maxwell's equations with no non-trivial null-spaces even on collocated grids. The ability to use non-staggered grids gives additional practical advantages, for example simplifying the treatment of complex geometry for high-order accurate numerical methods. More generally as discussed in [8], using the second-order formulation of wave equations has additional benefits including fewer dependent variables (e.g. from six to three for Maxwell's equations in three dimensions), and in some cases fewer constraint equations (e.g. the Saint-Venant compatibility conditions for linear elasticity).

For many physical applications, particularly electromagnetic propagation in matter, incorporation of dispersive effects arising from wave-matter interactions is critical. For time-domain problems, classical descriptions of the electron response (e.g. Drude, Drude-Lorentz, Lorentz, and Debye models) incorporate *ab initio* assumptions for interband and/or intraband electron transitions, as discussed for example in [2]. These classical models appear to possess some universality. For example, the same Lorentzian representation for the dielectric permittivity is capable of accurately approximating the optical dispersion due to phonon-polaritons excited with infrared light in SiC, or the interband electron transitions excited using ultraviolet light in metals. On the other hand, experimentally-based descriptions of dispersive dielectric functions given in the frequency domain are also broadly used. Such descriptions, for example, include polymeric relaxation behavior approximated by the Cole-Cole (C-C), Davidson-Cole (D-C), and Havriliak-Negami (H-N) models [9–12]. The C-C model is commonly utilized in biomedical electromagnetics for describing frequency dependent dielectric permittivity of human tissues [13], while in addition to the Debye and C-C models, the Jonscher approximation is often employed in the simulation of dispersive dielectric permittivity of concrete in civil and industrial engineering [14]. However, the need for fractional derivatives in the C-C, D-C, H-N, and Jonscher models significantly complicate their numerical implementations [15–17].

In order to numerically implement generic dispersive material models including classical descriptions derived from *ab initio* assumptions, or those fitted to experiment, we adopt a generalized dispersive material (GDM) model based on Padé approximants as described in [18]. In this approach, the frequency response of any material is approximated to arbitrary accuracy using a rational function of sufficiently high-order. This fitted frequency response is then transformed into the time-domain to yield either a time-delayed integral convolution equation, or a system of auxiliary ordinary differential equations. Numerical treatment of these two options are then classically referred to as either recursive convolution (RC) [19–23] or the auxiliary differential equation (ADE) method [23–28]. For *ab initio* dispersive models, various higher-order accurate numerical methods have been proposed using the ADE time-domain approach [29–33], while high-order schemes for Maxwell's equations in second-order form using RC were considered in [34]. On the other hand, second-order accurate RC- and ADE-type schemes for the solution of Maxwell's equations coupled to the GDM model were presented and analyzed in [18, 35]. Dispersive effects have also been incorporated into Maxwell's equations in first-order [36, 37] and second-order [38–40] form using a combination of finite-element and discontinuous Galerkin approaches with the ADE and RC coupling techniques. More sophisticated phenomenological hydrodynamic models for dispersion, their numerical implementation and comparison to experiments have also been addressed, e.g. [41–47] and references within.

In the current work, we consider higher-order accurate numerical methods for electromagnetic wave propagation and general dispersive materials on complex geometric domains. The new scheme builds upon the approach developed in [6] with significant extensions to model general dispersive materials in an efficient manner. The scheme retains only three time-levels for electric field and polarization vectors; this version is more memory efficient, especially when there are many polarization vectors, than alternative approaches that were also considered. In particular, we propose a finite difference time domain (FDTD) solver for Maxwell's equations coupled to the GDM model on non-Cartesian and overlapping grids. Maxwell's equations are solved in second-order form to avoid the need for grid staggering. Material dispersion is described with a general Padé approximant implemented through multiple polarization vectors, each of which satisfies and ADE. Some theoretical analysis of the material model is included to indicate when solutions to the coupled equations will grow, decay, or remain neutrally stable in time. We present efficient second- and fourth-order accurate algorithms which are centered in time and space. Both algorithms use only three time-levels for the electric field and each polarization vector, and are stable for a wide range of material parameters. In addition, the scheme is made stable and robust on overlapping grids through the use of a novel upwind dissipation based upon the upwind scheme for wave equations developed in [7, 8]. To the authors' knowledge, this is the first second- and fourth-order accurate FDTD scheme for a general dispersive model on curvilinear and overlapping grids. This is also the first fourth-order accurate scheme for a generalized model which incorporates the Drude, Drude-Lorentz, and critical point descriptions of dispersive media while at the same time addressing more complicated electric permittivity functions.

The remainder of the article is organized as follows. In Section 2 the governing equations for the ADE-GDM model are presented together with a discussion of the GDM model and its dispersion relation. Section 3 describes the second-order and fourth-order accurate numerical schemes while Section 4 describes details of the spatial approximations and overlapping grids. The stability of the numerical schemes is considered in Section 5. Numerical results are presented in Section 6 while conclusions are given in Section 7.

2. Governing Equations

Consider the solution to the time-domain Maxwell's equations in a domain Ω containing a linearly dispersive medium with negligible magnetic polarization so that $\mathbf{B} = \mu_0\mathbf{H}$. In this case, Maxwell's equations in first-order form are

$$\begin{aligned}
&\partial_t \mathbf{D} = \nabla \times \mathbf{H}, && \mathbf{x} \in \Omega, && \text{(1a)}\\
&\mu_0 \partial_t \mathbf{H} = -\nabla \times \mathbf{E}, && \mathbf{x} \in \Omega, && \text{(1b)}\\
&\nabla \cdot \mathbf{D} = 0, \quad \nabla \cdot \mathbf{H} = 0, && \mathbf{x} \in \Omega, && \text{(1c)}\\
&\mathbf{D} = \epsilon_0 \mathbf{E} + \mathbf{P}. && && \text{(1d)}
\end{aligned}$$

Here, $\mathbf{D} = \mathbf{D}(\mathbf{x}, t)$ is the displacement vector, $\mathbf{E} = \mathbf{E}(\mathbf{x}, t)$ is the electric field, $\mathbf{H} = \mathbf{H}(\mathbf{x}, t)$ is the magnetic field, $\mathbf{P} = \mathbf{P}(\mathbf{x}, t)$ is the electric polarization vector, and ϵ_0 and μ_0 are, respectively, the vacuum permittivity and permeability. The dispersive medium is modeled using the GDM model, as discussed in more detail in Section 2.1, and an ADE approach is used to describe the time evolution of the polarization vector. The second-order formulation of the governing equations is

$$\begin{aligned}
&\partial_t^2 \mathbf{E} = c^2 \Delta \mathbf{E} - \epsilon_0^{-1}\, \partial_t^2 \mathbf{P}, && \mathbf{x} \in \Omega, && && \text{(2a)}\\
&\partial_t^2 \mathbf{P}_m + b_{1,m} \partial_t \mathbf{P}_m + b_{0,m} \mathbf{P}_m = \epsilon_0 \big(a_{0,m} \mathbf{E} + a_{1,m} \partial_t \mathbf{E} \big), && \mathbf{x} \in \Omega, && m = 1, 2, \ldots, N_p, && \text{(2b)}\\
&\mathbf{P} = \sum_{m=1}^{N_p} \mathbf{P}_m. && && && \text{(2c)}
\end{aligned}$$

where $c^2 = 1/(\epsilon_0 \mu_0)$ is the nominal wave speed, and the total polarization vector, $\mathbf{P}$, is the sum of N_p component polarization vectors $\mathbf{P}_m$. Each $\mathbf{P}_m$ satisfies an ordinary differential equation (2b), whose coefficients $a_{0,m}$, $a_{1,m}$, $b_{0,m}$, and $b_{1,m}$ are chosen to fit a given dispersion model or spectroscopic data. For completeness we note that $\mathbf{H}$ satisfies the generalized second-order wave equation given by

$$\frac{1}{c^2}\, \partial_t^2 \mathbf{H} = \Delta \mathbf{H} + \nabla \times \partial_t \mathbf{P}. \tag{3}$$

The system of equations in (2) is augmented with appropriate initial conditions for $\mathbf{E}$ and $\mathbf{P}_m$ as

$$\begin{aligned}
&\mathbf{E}(\mathbf{x}, 0) = \mathbf{E}^0(\mathbf{x}), && \partial_t \mathbf{E}(\mathbf{x}, 0) = \mathbf{E}^1(\mathbf{x}), && \text{(4a)}\\
&\mathbf{P}_m(\mathbf{x}, 0) = \mathbf{P}_m^0(\mathbf{x}), && \partial_t \mathbf{P}_m(\mathbf{x}, 0) = \mathbf{P}_m^1(\mathbf{x}). && \text{(4b)}
\end{aligned}$$

In general, forcing functions can also be introduced into the equations and used as source terms but these are left off here to simplify the presentation. Boundary conditions are needed to close the system. For example the boundary conditions for a perfect electrical conductor (PEC) involve the tangential components of $\mathbf{E}$, which can be expressed as

$$\mathbf{n} \times \mathbf{E} = \mathbf{0}, \qquad \mathbf{x} \in \partial\Omega_{\text{PEC}}. \tag{5}$$

Note that the second-order order form of Maxwell's equations requires another boundary condition, and as in [6] we set the divergence of the field to be zero,

$$\nabla \cdot \mathbf{E} = 0, \qquad \mathbf{x} \in \partial\Omega_{\text{PEC}}. \tag{6}$$

Finally, note that since the equations for $\mathbf{P}_m$ are ODEs in time, no boundary conditions are needed on these components of the solution.

2.1. The generalized dispersion model in the frequency domain

The GDM model for the electric permittivity in the frequency domain, $\hat{\epsilon}$, takes the form

$$\hat{\epsilon}(\omega) = \epsilon_0\big(1 + \hat{\chi}(-i\omega)\big),$$

where the electric susceptibility $\hat{\chi}$ is given by

$$\hat{\chi}(s) \overset{\text{def}}{=} \sum_{m=1}^{N_p} \hat{\chi}_m(s), \tag{7a}$$

$$\hat{\chi}_m(s) \overset{\text{def}}{=} \frac{a_{0,m} + s\, a_{1,m}}{b_{0,m} + s\, b_{1,m} + s^2}. \tag{7b}$$

Given a representation for the susceptibility $\hat{\chi}(-i\omega)$ (from theory or experiment), the real-valued GDM coefficients $a_{0,m}$, $a_{1,m}$, $b_{0,m}$ and $b_{1,m}$ can be determined to fit the representation as a sum of Padé approximants of the form (7b) with N_p terms (see Appendix B for a discussion of determining the coefficients in the GDM model). Note that the classical Debye, Drude and Lorentz dispersion models are special cases of the GDM model. Note also that for the second-order form of the equations, electrical conductivity is given by a term $-\sigma\mathbf{E}_t$ which is added to the right-hand side of (2a). This term is a special case of (7b) with $a_{0,m} = b_{0,m} = b_{1,m} = 0$ and $a_{1,m} = \sigma$. Thus, conductivity, if present, could be treated separately for efficiency but here we do not do this as it simplifies the exposition of the algorithms.

To reveal the correspondence between (7) and (2), Fourier transform the relation (1d) for the displacement vector $\mathbf{D}$ in time to give

$$\hat{\mathbf{D}} = \epsilon_0\hat{\mathbf{E}} + \hat{\mathbf{P}},$$

where hats indicate the transformed variables, i.e. $\mathbf{E} = e^{-i\omega t}\hat{\mathbf{E}}$. Defining

$$\hat{\mathbf{P}} \overset{\text{def}}{=} \epsilon_0\, \hat{\chi}(-i\omega)\hat{\mathbf{E}}, \tag{8a}$$

$$\hat{\mathbf{P}}_m \overset{\text{def}}{=} \epsilon_0\hat{\chi}_m(-i\omega)\hat{\mathbf{E}}, \tag{8b}$$

leads to the expected relation

$$\hat{\mathbf{D}} = \hat{\epsilon}\,\hat{\mathbf{E}}.$$

Starting from (8b) and multiplying both sides by the denominator in (7b) for $\hat{\chi}_m(-i\omega)$, gives

$$-\omega^2\hat{\mathbf{P}}_m - i\omega\, b_{0,m}\hat{\mathbf{P}}_m + b_{0,m}\hat{\mathbf{P}}_m = \epsilon_0\big(a_{0,m}\hat{\mathbf{E}} - i\omega a_{1,m}\hat{\mathbf{E}}\big). \tag{9}$$

Transforming (9) back to the time domain gives the ADE (2b).

2.2. Dispersion relation for a general GDM model

The ADE-GDM equations for Maxwell's equations in second-order form are defined by the system in (2). The dispersion relation to these equations is found by seeking separable solutions of the form

$$\begin{aligned}\mathbf{E}(\mathbf{x},t) &= e^{st}e^{ikx}\,\hat{\mathbf{E}},\\ \mathbf{P}_m(\mathbf{x},t) &= e^{st}e^{ikx}\,\hat{\mathbf{P}}_m,\end{aligned}$$

for constants $s \in \mathbb{C}$ and $k \in \mathbb{C}$. Substituting this ansatz into (2) leads to the following relation between the polarization vectors $\mathbf{P}_m$, and the electric field $\mathbf{E}$,

$$\hat{\mathbf{P}}_m = \epsilon_0 \hat{\chi}_m(s)\,\hat{\mathbf{E}}, \qquad \hat{\mathbf{P}} = \sum_{m=1}^{N_p} \hat{\mathbf{P}}_m = \epsilon_0\,\hat{\chi}(s)\hat{\mathbf{E}}, \tag{10}$$

together with the dispersion relation

$$\big(s^2 + (ck)^2\big) + s^2 \sum_{m=1}^{N_p} \left\{ \frac{a_{0,m} + s a_{1,m}}{s^2 + b_{1,m}s + b_{0,m}} \right\} = 0. \tag{11}$$

Multiplying by the denominators in the sum in (11) yields a polynomial of degree $2N_p + 2$ in s:

$$\big(s^2 + (ck)^2\big) \prod_{j=1}^{N_p} \big(s^2 + b_{1,j}s + b_{0,j}\big) + s^2 \sum_{m=1}^{N_p} \left\{ \big(a_{0,m} + s a_{1,m}\big) \prod_{j=1, j\neq m}^{N_p} \big(s^2 + b_{1,j}s + b_{0,j}\big) \right\} = 0. \tag{12}$$

Given k, this polynomial can be solved to determine the roots s_n, $n = 1, 2, \ldots, 2N_p + 2$. For real k and real coefficients $a_{0,m}$, $a_{1,m}$, $b_{0,m}$ and $b_{1,m}$, the roots s_n appear as complex conjugate pairs corresponding to left- and right-traveling plane-wave solutions that decay in time when $\Re(s) < 0$ and grow in time when $\Re(s) > 0$. Alternatively, (11) can be solved for a given s to give two values of $k \in \mathbb{C}$,

$$(ck)^2 = -s^2 - s^2 \sum_{m=1}^{N_p} \left\{ \frac{a_{0,m} + s a_{1,m}}{s^2 + b_{1,m}s + b_{0,m}} \right\}. \tag{13}$$

When $s = \pm i\omega$, $\omega \in \mathbb{R}$, the solutions for k from (13) correspond to time-periodic solutions that decay or grow in space depending on the sign of $\Re(ikx)$, except for the constant solution when $\omega = 0$.

Resonant modes. Consider (13) with vanishing damping terms, $a_{1,m} = 0$, $b_{1,m} = 0$ so that

$$-(ck)^2 = s^2\Big(1 + \sum_{m=1}^{N_p} \frac{a_{0,m}}{s^2 + b_{0,m}}\Big). \tag{14}$$

When $|ck|$ is large (i.e. $|ck| \gg 1$), in order for the right-hand side of (14) to balance the left-hand side, it must be that either s^2, or one of the terms in the sum is large (assuming the $b_{0,m}$ are distinct). Therefore, for large $|ck|$ the roots to (14) take one of the following asymptotic forms

$$s^2 \sim -(ck)^2, \tag{15}$$

$$s_m^2 \sim -b_{0,m} + \frac{a_{0,m}\, b_{0,m}}{(ck)^2}, \quad m = 1, 2, \ldots, N_p. \tag{16}$$

The roots $s \sim \pm ick$ correspond to the usual wave modes for the non-dispersive Maxwell's equations with phase speed c. The roots $s_m \sim \pm i\sqrt{b_{0,m}}$ (assuming positive $b_{0,m}$) are the dispersive modes with phase speed $\sqrt{b_{0,m}}/k$ (i.e. slowly-moving waves). When $s_m \sim \pm i\sqrt{b_{0,m}}$ the polarization vector, $\hat{\mathbf{P}}_m$, given by

$$\hat{\mathbf{P}}_m = \frac{\epsilon_0 a_{0,m}}{s_m^2 + b_{0,m}} \hat{\mathbf{E}} \sim \frac{\epsilon_0 (ck)^2}{b_{0,m}} \hat{\mathbf{E}}, \tag{17}$$

has a large response, and thus $\omega \sim \sqrt{b_{0,m}}$, $m = 1, 2, \ldots, N_p$, represents the resonant frequencies of the dispersive model for $|ck|$ large.

Consider now the general case for $N_p = 1$ with non-zero damping coefficients. For clarity we drop the subscript m on $a_{1,m}$, b_{0m}, etc. The asymptotic forms for the roots for large ck are given by

$$s = \pm ick - \frac{a_1}{2} \mp \frac{i}{8ck}\Big(a_1^2 + 4a_1 b_1 - 4a_0\Big) + \mathcal{O}\big((ck)^{-2}\big), \tag{18}$$

$$s = r + \frac{1}{(ck)^2}\Big(\frac{-b_1^2 a_1 r + (ra_0 - a_1 b_0)b_1 + b_0(a_0 + ra_1)}{b_1 + 2r}\Big) + \mathcal{O}\big((ck)^{-4}\big), \tag{19}$$

where r is a root of $r^2 + b_1 r + b_0 = 0$. The first correction term for the non-resonant root in (18) is the addition of a negative real part, $-a_1/2$, which corresponds to damping in time; the second correction term in (18) incorporates a phase shift. The resonant mode s_m in (19) incorporates damping at the leading order term through the effect of b_1 on the root r; the first correction term in (19) adjusts both the real and imaginary parts of s, in general.

Conditions on the GDM parameters for non-growing solutions. Intuition suggests that $a_{1,m}$ and $b_{1,m}$ are coefficients of damping terms in the equations, and should normally be taken as non-negative to avoid exponential growth (gain materials could be modeled with negative values for $a_{1,m}$ or $b_{1,m}$). On the other hand, $\sqrt{a_{0,m}}$ and $\sqrt{b_{0,m}}$ change the phase (imaginary part of s) and thus should also be non-negative to avoid exponential growth. These conjectures are in agreement with the asymptotic formulae (15)–(16) and (18)–(19) (although the role of a_0 is only evident in the higher corrections). Despite this intuition and partial evidence, the model actually admits *bounded* exponential growth in the solution even for some cases where the constants $a_{0,m}$, $a_{1,m}$, $b_{0,m}$ and $b_{1,m}$, are all positive. To see this phenomenon, specialize to the case of one polarization vector, so that (12) becomes

$$\big(s^2 + (ck)^2\big)\,\big(s^2 + b_1 s + b_0\big) + s^2\big(a_0 + sa_1\big) = 0, \tag{20}$$

which is a quartic polynomial of the form

$$f(s) = s^4 + Bs^3 + Cs^2 + Ds + E = 0,$$

where

$$\begin{aligned} B &= b_1 + a_1, \\ C &= (ck)^2 + b_0 + a_0, \\ D &= (ck)^2 b_1, \\ E &= (ck)^2 b_0. \end{aligned}$$

Routh-Hurwitz theory [48] yields the following necessary and sufficient conditions for all roots to have a negative real part:

$$\begin{aligned} B &> 0, \\ E &> 0, \\ C - \frac{D}{B} &> 0, \\ D - \frac{BE}{C - \frac{D}{B}} &> 0. \end{aligned}$$

As shown in Appendix A, these conditions are satisfied if the GDM coefficients are positive *and*

$$(ck)^2 \left[(a_1 + b_1)(a_0 b_1 - a_1 b_0) + a_1 b_1 (ck)^2 \right] > 0. \tag{21}$$

Note that (21) may be violated if $a_0 b_1 < a_1 b_0$, depending on the value of $a_1 b_1 (ck)^2$.

Theorem 1. *A sufficient, but not necessary, condition for there to be no roots to the GDM dispersion-relation* (20) *with non-negative real part is that all coefficients are positive and*

$$a_0 b_1 > a_1 b_0. \tag{22}$$

When $a_0 b_1 < a_1 b_0$ there may be exponentially growing solutions to the ADE-GDM equations (this is confirmed by computations), which would generally occur for small values of k when

$$(a_1 + b_1)(a_0 b_1 - a_1 b_0) + a_1 b_1 (ck)^2 < 0.$$

It is important to note however, that the growth rate is bounded (for GDM coefficients of any sign) since the rate does not increase with k. This can be seen for the case of $N_p = 1$ from the asymptotic form of the roots for large ck in equations (18)–(19). The asymptotic formulae show that as $|k| \to \infty$, the real part of the non-resonant roots become bounded above by $-a_1/2$ while the resonant roots converge to the roots to $r^2 + b_1 r + b_0 = 0$. Thus the equations remain well-posed even in the presence of this growth. We note that Routh-Hurwitz conditions for more than one polarization vector become algebraically complex and deriving a simple condition for growth of the solution seems difficult. However, for given GDM parameters it is straightforward to check the conditions numerically for the polynomial (12) to determine whether a given model admits growing solutions.

3. Numerical Scheme

The numerical approximations of the ADE-GDM equations described in this manuscript are derived using a similar methodology as that described previously in [6] for the non-dispersive Maxwell's equations in second-order form. The construction uses a space-time procedure to develop single-stage schemes with arbitrarily high orders of accuracy in space and time using the electric field values at only three time levels. The approach is based on a Taylor series expansion of the solution in time, and uses a Cauchy-Kowalevski (Lax-Wendroff) procedure to convert higher-order temporal derivatives into spatial derivatives as determined by the governing PDEs. Higher-order schemes are derived hierarchically, with high-order accurate schemes building upon lower-order approximations. Spatial derivatives are then approximated using finite-differences on overlapping grids as discussed in Section 4. Overlapping grids are used to represent complex geometry with a set of structured curvilinear grids. Optimized versions of the numerical schemes are used for Cartesian grids, since and these can be orders of magnitude faster than the corresponding schemes for curvilinear grids. Since most of the domain is often covered with a background Cartesian grid, the cost of the overall scheme approaches that of the Cartesian-grid implementation as the grid is refined.

3.1. Second-order accurate scheme

We begin with a description of the second-order accurate scheme in d space dimensions. Let $\mathbf{x}_{\mathbf{j}} \in \mathbb{R}^d$ denote the grid-points on a structured grid, where $\mathbf{j} = (j_1, \ldots, j_d) \in \mathbb{Z}^d$ is a multi-index of integers. Let $\mathbf{E}_{\mathbf{j}}^n \approx \mathbf{E}(\mathbf{x}_{\mathbf{j}}, n\Delta t)$ and $\mathbf{P}_{m,\mathbf{j}}^n \approx \mathbf{P}_m(\mathbf{x}_{\mathbf{j}}, n\Delta t)$ denote grid functions that approximate $\mathbf{E}$ and $\mathbf{P}_m$ respectively. The second-order accurate approximation to (2a)-(2b) is given by

$$D_{+t}D_{-t}\mathbf{E}_{\mathbf{j}}^n = c^2\Delta_{2h}\mathbf{E}_{\mathbf{j}}^n - \epsilon_0^{-1}D_{+t}D_{-t}\mathbf{P}_{\mathbf{j}}^n, \tag{23a}$$

$$D_{+t}D_{-t}\mathbf{P}_{m,\mathbf{j}}^n + b_{1,m}D_{0t}\mathbf{P}_{m,\mathbf{j}}^n + b_{0,m}\mathbf{P}_{m,\mathbf{j}}^n = \check{a}_{0,m}\mathbf{E}_{\mathbf{j}}^n + \check{a}_{1,m}D_{0t}\mathbf{E}_{\mathbf{j}}^n, \tag{23b}$$

where

$$\mathbf{P}_{\mathbf{j}}^n \overset{\text{def}}{=} \sum_{m=1}^{N_p} \mathbf{P}_{m,\mathbf{j}}^n, \tag{24}$$

and $\check{a}_{0,m}$ and $\check{a}_{1,m}$ are the scaled GDM parameters

$$\check{a}_{0,m} \overset{\text{def}}{=} \epsilon_0\, a_{0,m}, \qquad \check{a}_{1,m} \overset{\text{def}}{=} \epsilon_0\, a_{1,m}. \tag{25}$$

Here Δ_{2h} denotes a second-order accurate approximation to the Laplace operator Δ, while D_{+t}, D_{-t}, and D_{0t} denote the usual forward, backward, and central divided difference approximations to the time derivative, as given by

$$D_{+t}\mathbf{W}^n \overset{\text{def}}{=} \frac{\mathbf{W}^{n+1} - \mathbf{W}^n}{\Delta t}, \quad D_{-t}\mathbf{W}^n \overset{\text{def}}{=} \frac{\mathbf{W}^n - \mathbf{W}^{n-1}}{\Delta t}, \quad D_{0t}\mathbf{W}^n \overset{\text{def}}{=} \frac{\mathbf{W}^{n+1} - \mathbf{W}^{n-1}}{2\Delta t}, \tag{26}$$

for a generic grid function $\mathbf{W}^n$ (with the spatial index suppressed). A second-order accurate approximation to the first time-derivative is $D_{0t}\mathbf{W}^n$, while

$$D_{+t}D_{-t}\mathbf{W}^n = \frac{\mathbf{W}^{n+1} - 2\mathbf{W}^n + \mathbf{W}^{n-1}}{\Delta t^2}, \tag{27}$$

is a second-order accurate approximation to the second time-derivative. The spatial approximation is described in detail in Section 4. The discrete approximations in (23) define a locally implicit system for the vector unknowns $\mathbf{E}_{\mathbf{j}}^{n+1}$ and $\mathbf{P}_{m,\mathbf{j}}^{n+1}$, $m = 1, \ldots, N_p$. For future notational convenience, the linear difference operator defining the solution to this system will be denoted $\mathbf{L}_{2h}$ so that the update can be expressed compactly as

$$\begin{bmatrix} \mathbf{E} \\ \mathbf{P}_m \end{bmatrix}_{\mathbf{j}}^{n+1} = \mathbf{L}_{2h}\left(\begin{bmatrix} \mathbf{E} \\ \mathbf{P}_m \end{bmatrix}_{\mathbf{j}}^{n}, \begin{bmatrix} \mathbf{E} \\ \mathbf{P}_m \end{bmatrix}_{\mathbf{j}}^{n-1} \right). \tag{28}$$

This operator takes the usual form of a standard explicit update equation for the wave equation as a 3-level scheme with a 3^d-point stencil. It is important to note that the components, $\mathbf{E}_{\mathbf{j}}^{n+1}$ and $\mathbf{P}_{m,\mathbf{j}}^{n+1}$, in (28) can be decoupled algebraically, which then leads to an efficient implementation of the update. Details of this efficient implementation of the time-stepping scheme are given in Appendix C.1.

3.2. Fourth-order accurate scheme

Higher-order accurate schemes can be defined using a modified equation approach starting from the second-order-accurate scheme given in (23). Taylor-series in time implies

$$D_{+t}D_{-t}\mathbf{W}(\mathbf{x}, t) = \partial_t^2\mathbf{W} + \frac{2\Delta t^2}{4!}\partial_t^4\mathbf{W} + \mathcal{O}(\Delta t^4). \tag{29}$$

where $\mathbf{W}$ represents either $\mathbf{E}$ or $\mathbf{P}$. Time differentiation of the governing equations (2) yields

$$\partial_t^4\mathbf{E} = (c^2\Delta)^2\mathbf{E} - \epsilon_0^{-1}c^2\Delta\partial_t^2\mathbf{P} - \epsilon_0^{-1}\partial_t^4\mathbf{P}, \tag{30}$$

which are used to replace time-derivatives of $\mathbf{E}$ to give

$$D_{+t}D_{-t}\mathbf{E} = c^2\Delta\mathbf{E} - \epsilon_0^{-1}\partial_t^2\mathbf{P} + \frac{\Delta t^2}{12}\left[(c^2\Delta)^2\mathbf{E} - \epsilon_0^{-1}c^2\Delta\partial_t^2\mathbf{P} - \epsilon_0^{-1}\partial_t^4\mathbf{P}\right] + \mathcal{O}(\Delta t^4). \tag{31}$$

For fourth-order accuracy, the continuous temporal operators on the right-hand side of (31) are approximated using

$$\begin{aligned} \partial_t^2\mathbf{P} &= D_{+t}D_{-t}\left(1 - \frac{\Delta t^2}{12}D_{+t}D_{-t}\right)\mathbf{P} + \mathcal{O}(\Delta t^4), \\ \partial_t^4\mathbf{P} &= (D_{+t}D_{-t})^2\mathbf{P} + \mathcal{O}(\Delta t^2), \end{aligned}$$

which after spatial discretization yields

$$D_{+t}D_{-t}\mathbf{E}_{\mathbf{j}}^n = c^2\Delta_{4h}\mathbf{E}_{\mathbf{j}}^n - \epsilon_0^{-1}D_{+t}D_{-t}\mathbf{P}_{\mathbf{j}}^n + \frac{\Delta t^2}{12}\left((c^2\Delta_{2h})^2\mathbf{E}_{\mathbf{j}}^n - \epsilon_0^{-1}c^2\left[\Delta_{2h}\partial_t^2\mathbf{P}^*\right]_{\mathbf{j}}^n\right). \tag{32}$$

Here Δ_{4h} denotes a fourth-order accurate approximation to the Laplace operator Δ, and the blue "star" terms in square braces are needed only to second-order accuracy because they appear as $\mathcal{O}(\Delta t^2)$ corrections. This term is therefore evaluated using an explicit prediction from the second-order-accurate scheme as

$$\left[\Delta_{2h}\partial_t^2\mathbf{P}^*\right]_{\mathbf{j}}^n = \Delta_{2h}\left(\frac{\mathbf{P}_{\mathbf{j}}^{*n+1} - 2\mathbf{P}_{\mathbf{j}}^n + \mathbf{P}_{\mathbf{j}}^{n-1}}{\Delta t^2}\right), \tag{33}$$

where

$$\begin{bmatrix}\mathbf{E}^*\\ \mathbf{P}_m^*\end{bmatrix}_{\mathbf{j}}^{n+1} = \mathbf{L}_{2h}\left(\begin{bmatrix}\mathbf{E}\\ \mathbf{P}_m\end{bmatrix}_{\mathbf{j}}^{n}, \begin{bmatrix}\mathbf{E}\\ \mathbf{P}_m\end{bmatrix}_{\mathbf{j}}^{n-1}\right). \tag{34}$$

Similar manipulations yield a fourth-order accurate update equation for the $\mathbf{P}_{m,\mathbf{j}}$ equation as

$$\begin{aligned}
D_{+t}D_{-t}\mathbf{P}_{m,\mathbf{j}}^n = {}& -b_{1,m}\Big(D_{0t}\mathbf{P}_{m,\mathbf{j}}^n - \frac{\Delta t^2}{6}\left[\partial_t^3\mathbf{P}_m^*\right]_{\mathbf{j}}^n\Big) - b_{0,m}\mathbf{P}_{m,\mathbf{j}}^n \\
&+ \check{a}_{0,m}\mathbf{E}_{\mathbf{j}}^n + \check{a}_{1,m}\Big(D_{0t}\mathbf{E}_{\mathbf{j}}^n - \frac{\Delta t^2}{6}\left[\partial_t^3\mathbf{E}^*\right]_{\mathbf{j}}^n\Big) \\
&+ \frac{\Delta t^2}{12}\Big(- b_{1,m}\left[\partial_t^3\mathbf{P}_m^*\right]_{\mathbf{j}}^n - b_{0,m}D_{+t}D_{-t}\mathbf{P}_{m,\mathbf{j}}^n \\
&\qquad + \check{a}_{0,m}D_{+t}D_{-t}\mathbf{E}_{\mathbf{j}}^n + \check{a}_{1,m}\left[\partial_t^3\mathbf{E}^*\right]_{\mathbf{j}}^n\Big),
\end{aligned} \tag{35}$$

where again the blue "star" terms in square braces are evaluated using explicit predictions from the second-order-accurate scheme. The ADE (2b) can be used to recursively replace second-order (or higher) temporal derivatives of $\mathbf{P}_m$ in terms of lower-order derivatives so that $\partial_t^3\mathbf{P}_m$ can be written as

$$\partial_t^3\mathbf{P}_m = b_{1,m}^{(3)}\partial_t\mathbf{P}_m + b_{0,m}^{(3)}\mathbf{P}_m + \check{a}_{0,m}^{(3)}\mathbf{E} + \check{a}_{1,m}^{(3)}\partial_t\mathbf{E} + \check{a}_{2,m}^{(3)}\partial_t^2\mathbf{E}, \tag{36}$$

where

$$b_{1,m}^{(3)} = (b_{1,m}^2 - b_{0,m}), \qquad b_{0,m}^{(3)} = b_{1,m}b_{0,m},$$
$$\check{a}_{0,m}^{(3)} = -\check{a}_{0,m}b_{1,m}, \qquad \check{a}_{1,m}^{(3)} = (\check{a}_{0,m} - \check{a}_{1,m}b_{1,m}), \qquad \check{a}_{2,m}^{(3)} = \check{a}_{1,m}.$$

Equation (36) could be discretized directly at second-order. However, for the purposes of simplifying the implementation for the case of multiple polarization vectors, we find it advantageous to again use the second-order scheme to predict values at the new time prior to time discretization of (36). In this way, $\left[\partial_t^3\mathbf{P}_m^*\right]_{\mathbf{j}}^n$ in (35) is defined as

$$\left[\partial_t^3\mathbf{P}_m^*\right]_{\mathbf{j}}^n = b_{1,m}^{(3)}\left[\partial_t\mathbf{P}_m^*\right]_{\mathbf{j}}^n + b_{0,m}^{(3)}\mathbf{P}_{m,\mathbf{j}} + \check{a}_{0,m}^{(3)}\mathbf{E}_{\mathbf{j}} + \check{a}_{1,m}^{(3)}\left[\partial_t\mathbf{E}^*\right]_{\mathbf{j}}^n + \check{a}_{2,m}^{(3)}\left[\partial_t^2\mathbf{E}^*\right]_{\mathbf{j}}^n. \tag{37}$$

where

$$\big[\partial_t \mathbf{P}_m^*\big]_{\mathbf{j}}^n = \frac{\mathbf{P}_{m,\mathbf{j}}^{*\,n+1} - \mathbf{P}_{m,\mathbf{j}}^{n-1}}{2\Delta t}, \tag{38a}$$

$$\big[\partial_t \mathbf{E}^*\big]_{\mathbf{j}}^n = \frac{\mathbf{E}_{\mathbf{j}}^{*\,n+1} - \mathbf{E}_{\mathbf{j}}^{n-1}}{2\Delta t}, \tag{38b}$$

$$\big[\partial_t^2 \mathbf{E}^*\big]_{\mathbf{j}}^n = \frac{\mathbf{E}_{\mathbf{j}}^{*\,n+1} - 2\mathbf{E}_{\mathbf{j}}^{n} - \mathbf{E}_{\mathbf{j}}^{n-1}}{\Delta t^2}. \tag{38c}$$

The approach to approximating $\big[\partial_t^3 \mathbf{E}^*\big]_{\mathbf{j}}^n$ in (35) follows similar steps to yield

$$\big[\partial_t^3 \mathbf{E}^*\big]_{\mathbf{j}}^n = c^2\big[\Delta_{2h}\partial_t \mathbf{E}^*\big]_{\mathbf{j}}^n - \epsilon_0^{-1}\big[\partial_t^3 \mathbf{P}^*\big]_{\mathbf{j}}^n, \tag{39}$$

where, as before, $\big[\Delta_{2h}\partial_t \mathbf{E}^*\big]_{\mathbf{j}}^n$ uses the second-order approximation

$$\big[\Delta_{2h}\partial_t \mathbf{E}^*\big]_{\mathbf{j}}^n = \frac{\Delta_{2h}\mathbf{E}_{\mathbf{j}}^{*\,n+1} - \Delta_{2h}\mathbf{E}_{\mathbf{j}}^{n-1}}{2\Delta t}, \tag{40}$$

with $\mathbf{E}_{\mathbf{j}}^{*\,n+1}$ obtained from (34).

To summarize the fourth-order scheme, the approximations in (32) and (35) determine the updates for $\mathbf{E}_{\mathbf{j}}^{n+1}$ and $\mathbf{P}_{m,\mathbf{j}}^{n+1}$, with the summation of the latter quantity giving $\mathbf{P}_{\mathbf{j}}^{n+1}$. Similar to the second-order case, this linear difference operator will be denoted

$$\begin{bmatrix} \mathbf{E} \\ \mathbf{P}_m \end{bmatrix}_{\mathbf{j}}^{n+1} = \mathbf{L}_{4h}\left(\begin{bmatrix} \mathbf{E} \\ \mathbf{P}_m \end{bmatrix}_{\mathbf{j}}^{n}, \begin{bmatrix} \mathbf{E} \\ \mathbf{P}_m \end{bmatrix}_{\mathbf{j}}^{n-1} \right), \tag{41}$$

which ultimately takes the form of a standard explicit update equation for the wave equation as a 3-level scheme with a 5^d-point stencil. Note that embedded in the operator $\mathbf{L}_{4h}$ are explicit evaluations of the correction terms $\big[\partial_t \mathbf{E}^*\big]_{\mathbf{j}}^n$, $\big[\Delta_{2h}\partial_t \mathbf{E}^*\big]_{\mathbf{j}}^n$, etc., using the second-order scheme $\mathbf{L}_{2h}$. Therefore, the $\mathbf{L}_{4h}$ operator can be evaluated by explicit inversion of the system as in the second-order case. See Appendix C for further details of this efficient implementation. Finally, we note that it also appears possible to define a scheme that introduces new unknowns defining the time-derivatives of $\mathbf{P}_{m,\mathbf{j}}$ such as $\mathbf{Q}_m \overset{\text{def}}{=} \partial_t^2 \mathbf{P}_{m,\mathbf{j}}$. This leads to an algebraically simpler scheme, but at the cost of requiring additional storage for $\mathbf{Q}_m$, and so we have not pursued this approach.

4. Spatial approximations and composite grids

The ADE-GDM schemes presented in Section 3 are defined in terms of generic spatial approximations for the Laplace operator and the square of the Laplace operator. While there are a variety of approaches that can be used to approximate these operators, our approach employs finite-difference approximations on overlapping grids. In the discussion below, we provide a brief description of the overlapping grid approach and the approximation of the Laplace operator. This is followed by a discussion of the upwind dissipation used to suppress numerical instabilities at overlapping-grid boundaries, and the numerical treatment of the boundary conditions at a perfect electrical conductor (PEC) boundary.

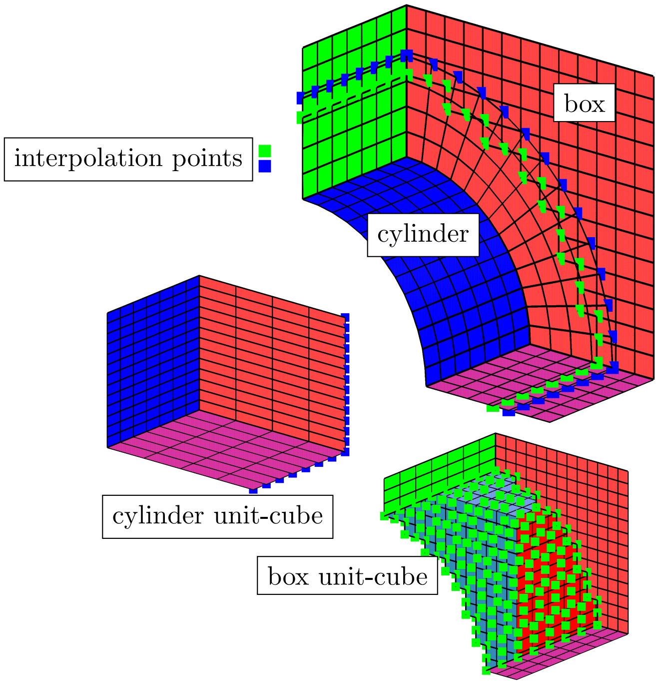

Figure 1: Top: a three-dimensional overlapping grid for a quarter-cylinder in a box. Bottom left and right: component grids for the cylindrical and box grids in the unit cube parameter space. Interpolation points at the grid overlap are marked and color-coded for each component grid.

4.1. Composite grids for complex geometry

As illustrated in Figure 1, a composite overlapping grid, denoted as $\mathcal{G}$, consists of a set of component grids $\mathcal{G}_g$, $g = 1, \ldots, \mathcal{N}$, that cover the entire domain Ω. In three dimensions, each component grid, $\mathcal{G}_g$, is a logically rectangular, curvilinear grid defined by a smooth mapping from a unit cube parameter space $\mathbf{r}$ to physical space $\mathbf{x}$,

$$\mathbf{x} = \mathbf{G}_g(\mathbf{r}, t), \qquad \mathbf{r} \in [0,1]^3, \qquad \mathbf{x} \in \mathbb{R}^3. \tag{42}$$

The overlapping grid generator **Ogen** [49] from the *Overture* framework is used to construct the overlapping grid information. In a typical composite grid, one or more boundary-fitted curvilinear grids represents each boundary. The remainder of the domain is covered by one or more Cartesian grids. **Ogen** cuts holes in the appropriate component grids by using physical boundaries to distinguish between the interior and exterior to the domain. For example, the “cylinder” grid displayed in the upper right image of Figure 1 cuts a hole in the Cartesian “box” grid so that the latter grid has many unused points (those not being plotted in the lower right image). **Ogen** also provides the interpolation information for all interpolation points in the overlap region between component grids. The interpolation between grids is defined using tensor-product Lagrange interpolation in the parameter space of the mapping $\mathbf{G}_g$. The unit square coordinates $\mathbf{r}$ of a given point $\mathbf{x}$ on one grid are located in the donor-grid parameter space. The interpolation is performed in the Cartesian-grid parameter space and is thus straightforward [50]. The width of the interpolation depends on the order of accuracy of the scheme. For fourth-order accuracy, for example, a five-point wide interpolation stencil is used, and two layers of interpolation points are required to support the five-point stencil.

4.2. Finite-difference approximations on overlapping grids

The ADE-GDM scheme is discretized in space using finite-difference approximations. We require second- and fourth-order accurate compact-stencil approximations to the Laplace operator,

$$L \overset{\text{def}}{=} \Delta = \sum_{\mu=1}^{d} \frac{\partial^2}{\partial x_\mu^2}. \tag{43}$$

Each component grid of the overlapping grid is defined by a smooth invertible mapping $\mathbf{x} = \mathbf{G}_g(\mathbf{r})$, where $\mathbf{r} \in [0,1]^d$ denotes the unit parameter-space coordinate-vector in d space dimensions. Using the chain rule, an exact transformation of the derivatives in (43) from physical space to parameter space is performed. This transformation involves metrics of the mapping, and their derivatives, and this information is supplied by the grid generator. The first and second derivatives with respect to the parameter-space coordinates that appear in the transformation of the Laplacian are approximated to the desired order of accuracy, either second- or fourth-order accuracy, using standard centered differences, see [50] for example.

4.3. Upwind dissipation

A high-order upwind dissipation is added to the centered approximation in order to eliminate instabilities that may arise from the interpolation between overlapping grids. For efficiency we often use *thin* boundary-fitted grids at curved boundaries with a fixed number of grid points in the direction normal to the boundary. As a result, the majority of the domain is covered by efficient Cartesian component grids as the grids are refined. However, this choice means that the interpolation interface approaches the physical boundary as the grids are refined, which is known to excite numerical instabilities, as discussed, for example, in [7, 51]. It was shown in [51] that typical artificial dissipation operators used to guard against these instabilities are ineffective unless the coefficient determining the strength of the dissipation scales inversely proportionally to the grid spacing. This scaling would thus lead to a loss in the observed order of accuracy. In [7] a high-order upwind scheme was presented for the wave equation on overlapping grids and applied to Maxwell's equations in second-order form. Upwinding was incorporated by embedding an exact solution to a local Riemann problem into the scheme. The scheme was shown to be robustly stable and fully accurate even in the difficult case of instabilities caused by interpolation at thin boundary-fitted grids. In follow up work [52], a reformulation of the scheme incorporated several optimizations that led to a new method where the upwind term that ultimately contributes numerical dissipation is separated from the wave operator. This observation was leveraged to give an effective dissipation term that can be added readily to existing wave equation solvers. The approach has no free tunable parameters, and the upwind dissipation is effective at eliminating numerical instabilities caused by overlapping grid interpolation.

The dissipation operator suggested by the approach in [52] is used in the present scheme. For the fourth-order accurate scheme, for example, the upwind dissipation takes the form

$$\mathcal{D}^{(4)}\mathbf{E}_{\mathbf{j}}^n \overset{\text{def}}{=} \delta^{(4)} \sum_{l=1}^{d} h_l^5 (D_{+l}D_{-l})^3 D_{0t}\mathbf{E}_{\mathbf{j}}^n. \tag{44}$$

Here, $\delta^{(4)}$ is the coefficient of the dissipation, h_l is the grid spacing is the r_l parameter-space coordinate direction, and D_{+l} and D_{-l} denote the usual forward and backward divided-difference operators defined by

$$D_{+l} w_{\mathbf{j}} \overset{\text{def}}{=} \frac{w_{\mathbf{j}+\mathbf{e}_l} - w_{\mathbf{j}}}{h_l}, \qquad D_{-l} w_{\mathbf{j}} \overset{\text{def}}{=} \frac{w_{\mathbf{j}} - w_{\mathbf{j}-\mathbf{e}_l}}{h_l}, \tag{45}$$

where $\mathbf{e}_l$ is the unit vector in r_l-direction, e.g. $\mathbf{e}_2 = [0, 1, 0]^T$ for $d = 3$. Following the approach in [52], the coefficient of the dissipation is taken to be $\delta^{(4)} = 5c/288$, which is given automatically by the construction of the dissipation, and in general varies with the order of accuracy. For this fourth-order accurate scheme, the dissipation stencil is seven-points wide (compared to the five-point $\mathbf{L}_{4h}$ operator), and so one additional ghost point is needed at physical boundaries. The dissipation in (44) scales as $\mathcal{O}(h_l^5)$ for well-resolved modes of the solution, and thus does not affect the overall fourth-order accuracy of the scheme. As discussed in [52], the dissipation is added in a predictor-corrector fashion since this allows for a larger time-step. The solution is first advanced with the base scheme in the predictor stage and then the dissipation is added in the corrector stage,

$$\mathbf{E}_{\mathbf{j}}^n \leftarrow \mathbf{E}_{\mathbf{j}}^n + \Delta t \, \mathcal{D}^{(4)} \mathbf{E}_{\mathbf{j}}^{n-1}.$$

A further discussion of a stable choice for the time-step is given in Section 5 below.

4.4. Boundary Conditions

In this section, we describe the numerical implementation of the boundary conditions at a PEC boundary. The primary boundary conditions, given previously in (5) and (6), are

$$\mathbf{n} \times \mathbf{E} = 0, \qquad \mathbf{x} \in \partial\Omega_{\text{PEC}}, \tag{46a}$$

$$\nabla \cdot \mathbf{E} = 0, \qquad \mathbf{x} \in \partial\Omega_{\text{PEC}}, \tag{46b}$$

respectively, setting the right-side forcing function in (5) to be zero. Since the ADE-GDM governing equations in (2) involve no spatial derivatives of $\mathbf{P}_m$, there are no boundary conditions required for $\mathbf{P}_m$ at the continuous level. The condition in (46a) specifies the tangential components of $\mathbf{E}$ on the boundary. A second-order accurate centered approximation of (46b) gives the normal component of $\mathbf{E}$ in the first ghost line, while the tangential components of $\mathbf{E}$ can be obtained in the first ghost line using extrapolation. This is sufficient for the implementation of the second-order accurate scheme described in Section 3.1 without upwind dissipation. When the dissipation is included, values of $\mathbf{E}$ are required at a second ghost line and these are obtained using extrapolation.

For the fourth-order accurate scheme discussed in Section 3.2, additional values involving both $\mathbf{E}$ and $\mathbf{P}_m$ are needed on ghost lines. These values may be obtained from compatibility conditions derived at a continuous level from the governing equations and boundary conditions. For example, taking the divergence of (2b) and evaluating the result on the boundary implies

$$\frac{\partial^2 (\nabla \cdot \mathbf{P}_m)}{\partial t^2} + b_{1,k} \frac{\partial (\nabla \cdot \mathbf{P}_m)}{\partial t} + b_{0,k} (\nabla \cdot \mathbf{P}_m) = 0, \qquad \mathbf{x} \in \partial\Omega_{\text{PEC}}, \tag{47}$$

since $\nabla \cdot \mathbf{E} = 0$ and $\partial_t (\nabla \cdot \mathbf{E}) = 0$ on the boundary. Assuming that $\nabla \cdot \mathbf{P}_m = 0$ and $\partial_t (\nabla \cdot \mathbf{P}_m) = 0$ initially, then (47) implies that

$$\nabla \cdot \mathbf{P}_m = 0, \qquad \mathbf{x} \in \partial\Omega_{\text{PEC}}. \tag{48}$$

A similar argument gives

$$\mathbf{n} \times \mathbf{P}_m = 0, \qquad \mathbf{x} \in \partial\Omega_{\text{PEC}}, \tag{49}$$

which implies that the tangential components of $\mathbf{P}_m$ are also zero on a PEC boundary.

Additional compatibility conditions for $\mathbf{E}$ at PEC boundaries are derived following the approach in [6] by taking time-derivatives of the governing equations. For example, taking two time derivatives of (2a) and using (46a) implies

$$c^2\mathbf{n} \times \Delta\mathbf{E} = -\epsilon_0^{-1}\frac{\partial^4(\mathbf{n}\times\mathbf{P})}{\partial t^4} = 0, \qquad \mathbf{x} \in \partial\Omega_{\text{PEC}},$$

which is the same condition for $\mathbf{E}$ as in the non-dispersive case. It then follows by applying $\mathbf{n} \times \Delta$ to (2a) for $\mathbf{P}_m$ that

$$\mathbf{n} \times \Delta\mathbf{P}_m = 0, \qquad \mathbf{x} \in \partial\Omega_{\text{PEC}}, \tag{50}$$

and thus $\mathbf{P}_m$ satisfies the same compatibility condition as $\mathbf{E}$. In general, $\mathbf{P}_m$ will satisfy the same compatibility conditions for $\mathbf{E}$ at a PEC boundary (see [6] for the general conditions).

When there are a large number of polarization vectors, an application of the full compatibility boundary conditions for all $\mathbf{P}_m$, $m = 1, \ldots, N_p$, may become expensive. Therefore, we currently only impose (49) as a primary compatibility boundary condition for $\mathbf{P}_m$, but do not use compatibility conditions in (48) or (50). Instead, the ghost points values for $\mathbf{P}_m$ are simply obtained by extrapolation (which appears to be effective in practice). For example,

$$D_{+l}^{q}\mathbf{P}_{m,\mathbf{j}}^{n} = 0, \quad \text{for a ghost point } \mathbf{j},$$

defines a q-point extrapolation formula. For the second-order accurate scheme, q is taken as three while for the fourth-order accurate scheme, q is taken as five.

5. Stability

We now examine the stability and accuracy of the second- and fourth-order accurate ADE-GDM schemes. The analysis considers the case of one polarization vector, i.e. $N_p = 1$, and assumes that the damping coefficients, a_1 and b_1, in (2b) are zero. Our motivation for these choices is to make the details of the analysis as simple as possible. Also, with the damping coefficients equal to zero, there is no mechanism for decay in the exact solution of the equations which could provide a corresponding damping in the numerical scheme. In fact, we find, as discussed below, that the two numerical schemes described in Section 3 is neutrally stable for a suitable CFL time-step. The numerical results discussed later in this section confirm the analysis and provide evidence of the stability in the case with nonzero damping coefficients.

5.1. Stability of the second-order accurate ADE-GDM scheme

The stability of the second-order accurate ADE-GDM scheme can be studied using a von Neumann analysis. We consider a square domain $\Omega = [0, 2\pi]^d$, discretized with a Cartesian grid, and examine 2π-periodic solutions. A second-order accurate approximation to the Laplacian is given by

$$\Delta_{2h} \overset{\text{def}}{=} \sum_{l=1}^{d} D_{+l} D_{-l},$$

where the grid spacing, h_l, given in the definitions of the divided difference operators in (45) are now scaled by 2π. We seek solutions to the difference approximation (23) of the form

$$\mathbf{E}_{\mathbf{j}}^n = A^n \, e^{i\mathbf{k}\cdot\mathbf{x}_{\mathbf{j}}} \, \hat{\mathbf{E}}, \tag{51a}$$

$$\mathbf{P}_{\mathbf{j}}^n = A^n \, e^{i\mathbf{k}\cdot\mathbf{x}_{\mathbf{j}}} \, \hat{\mathbf{P}}, \tag{51b}$$

where A denotes the amplification factor and $\mathbf{k}$ is a wave-number vector. Substitution of the ansatz (51) into (23) gives

$$\left[\frac{A - 2 + A^{-1}}{\Delta t^2} + c^2 \hat{L}_{2h}(\mathbf{k}) \right] \hat{\mathbf{E}} = -\epsilon_0^{-1} \frac{A - 2 + A^{-1}}{\Delta t^2} \, \hat{\mathbf{P}}, \tag{52a}$$

$$\left[\frac{A - 2 + A^{-1}}{\Delta t^2} + b_0 \right] \hat{\mathbf{P}} = \epsilon_0 \, a_0 \hat{\mathbf{E}}, \tag{52b}$$

where

$$\hat{L}_{2h}(\mathbf{k}) \overset{\text{def}}{=} \sum_{l=1}^{d} \frac{4 \sin^2(\xi_l/2)}{h_l^2}, \qquad \xi_l \overset{\text{def}}{=} k_l h_l \in [-\pi, \pi]. \tag{53}$$

Equation (52b) is used to solve for $\hat{\mathbf{P}}$ in terms of $\hat{\mathbf{E}}$, and this is substituted into (52a) to give the following equation for the amplification factor A:

$$\left[\frac{A - 2 + A^{-1}}{\Delta t^2} + c^2 \hat{L}_{2h}(\mathbf{k}) \right] \left[\frac{A - 2 + A^{-1}}{\Delta t^2} + b_0 \right] + a_0 \left(\frac{A - 2 + A^{-1}}{\Delta t^2} \right) = 0. \tag{54}$$

Multiplying (54) by A^2 gives a polynomial equation for A of degree four. Since the coefficients in the polynomial are all real, the four roots will be either real, or they will appear as complex conjugate pairs which we denote by A and $\bar{A}$, respectively.

The number of roots for A is the same as the number of roots s of the corresponding analytic dispersion relation in (20) with the damping coefficients set to zero. Thus, there are no spurious roots for A. For well-resolved modes with $\Delta t \to 0$ and $c^2 \hat{L}_{2h}(\mathbf{k}) \Delta t^2 \to 0$, it is straightforward to show that the solutions of (54) take the form

$$A = 1 + s\Delta t + \frac{1}{2}(s\Delta t)^2 + \mathcal{O}(\Delta t^3), \tag{55}$$

where s is a root of the corresponding continuous dispersion relation (20). This confirms that the scheme is second-order accurate since A should be an approximation to $e^{s\Delta t}$.

For stability we require $|A| \leqslant 1$ if A is an isolated root, and $|A| < 1$ if A is a multiple root. We now show that the second-order accurate ADE-GDM scheme is neutrally stable under a reasonably CFL time-step constraint.

The constraint in (54) for the amplification factor A of the second-order accurate scheme can be written as

$$P_0(A) \overset{\text{def}}{=} \Big[\big(A-2+A^{-1}\big)+c^2\Delta t^2\hat{L}_{2h}(\mathbf{k})\Big]\Big[\big(A-2+A^{-1}\big)+\Delta t^2\,b_0\Big] \\ +\Delta t^2 a_0\left(A-2+A^{-1}\right)=0, \tag{56}$$

which is a quadratic in $A-2+A^{-1}$. Letting

$$A-2+A^{-1}=-4R, \tag{57}$$

we find that there are two roots for A,

$$A=1-2R\pm\sqrt{(1-2R)^2-1}, \tag{58}$$

for a given value of R. For $|A|\leqslant 1$, and to avoid the case of a double roots for A, it is sufficient to require that $(1-2R)^2<1$ in (58), in which case $|A|=1$. Thus, the stability condition is

$$0<R<1 \quad\rightarrow\quad |A|=1. \tag{59}$$

Therefore, when $0<R<1$, there is no damping in the discrete solution (when $R=0$ or $R=1$ there is a double root for A and we exclude these cases). Substituting (57) into (56) leads to

$$\Big[R-c^2\Delta t^2\hat{L}_{2h}(\mathbf{k})/4\Big]\Big[R-b_0\Delta t^2/4\Big]-R\left(a_0\Delta t^2/4\right)=0. \tag{60}$$

Equation (60) is a quadratic equation in R, which may be expressed as

$$R^2-2BR+C=0,$$

where

$$B=\frac{\Delta t^2}{8}(c^2\hat{L}_{2h}(\mathbf{k})+b_0+a_0), \qquad C=\frac{\Delta t^4}{16}(c^2\hat{L}_{2h}(\mathbf{k})\,b_0).$$

The roots of the quadratic are given by

$$R=B\pm\sqrt{B^2-C}. \tag{61}$$

For stability, we require $0<R<1$ which will be true when $0\leqslant C\leqslant B^2$ and

$$B+\sqrt{B^2-C}<1. \tag{62}$$

Note that $B^2-C\geqslant 0$ since

$$\begin{aligned} B^2-C &= \frac{\Delta t^4}{64}\left[\left(c^2\hat{L}_{2h}(\mathbf{k})+b_0+a_0\right)^2-4\left(c^2\hat{L}_{2h}(\mathbf{k})\,b_0\right)\right] \\ &= \frac{\Delta t^4}{64}\left[\left(c^2\hat{L}_{2h}(\mathbf{k})-b_0\right)^2+2\left(c^2\hat{L}_{2h}(\mathbf{k})+b_0\right)a_0+a_0^2\right]\geqslant 0. \end{aligned}$$

Since $C \geqslant 0$ and $\sqrt{B^2 - C} \leqslant B$, a sufficient condition for stability from (62) is $2B < 1$, and so

$$\Delta t^2 \left[\frac{1}{4} c^2 \hat{L}_{2h}(\mathbf{k}) + \frac{1}{4} (b_0 + a_0) \right] < 1. \tag{63}$$

Noting that

$$0 \leqslant \hat{L}_{2h}(\mathbf{k}) \leqslant 4 \sum_{l=1}^{d} \frac{1}{h_l^2}, \tag{64}$$

it follows that a sufficient condition for stability is

$$\Delta t^2 \left[c^2 \sum_{l=1}^{d} \frac{1}{h_l^2} + \frac{1}{4} (b_0 + a_0) \right] < 1. \tag{65}$$

This result is expressed in the following theorem.

Theorem 2. *The second-order accurate ADE-GDM scheme for one polarization vector ($N_p = 1$) and zero damping coefficients ($a_1 = b_1 = 0$), and with non-negative values for a_0 and b_0 is neutrally stable provided*

$$\Delta t < \left[c^2 \sum_{l=1}^{d} \frac{1}{h_l^2} + \frac{1}{4} (b_0 + a_0) \right]^{-1/2}. \tag{66}$$

It is noted that the GDM coefficients b_0 and a_0 will generally have negligible effect on the time-step as the mesh is refined, and thus in practice the time-step can be chosen from the usual non-dispersive condition,

$$\Delta t \leqslant \frac{C_{\text{cfl}}}{\sqrt{c^2 \sum_{l=1}^{d} \frac{1}{h_l^2}}}, \tag{67}$$

with a *safety factor*, $C_{\text{cfl}} = 0.9$, for example.

Note. We expect that (67), with $C_{\text{cfl}} = 0.9$, will also give a practical choice of the time-step for the general case with one or more polarization vectors and any non-negative GDM coefficients, including the damping coefficients.

5.2. Stability of the fourth-order accurate ADE-GDM scheme

Consider now the stability of the fourth-order accurate ADE-GDM scheme given in Section 3.2. As noted previously for the second-order scheme, we consider the case of one polarization vector ($N_p = 1$), zero damping coefficients in the GDM model ($a_1 = b_1 = 0$), and use the domain $\Omega = [0, 2\pi]^d$ with periodic boundaries. The fourth-order accurate scheme is applied on a Cartesian grid for which the spatial discretizations is

$$\Delta_{4h} \overset{\text{def}}{=} \sum_{l=1}^{d} D_{+l} D_{-l} \left(I - \frac{h_l^2}{12} D_{+l} D_{-l} \right).$$

Using the ansatz in (51) gives

$$\left[\frac{A-2+A^{-1}}{\Delta t^2}+\hat{\mathcal{L}}_h(\mathbf{k})-\frac{(c\Delta t)^2}{12}\,a_0\hat{L}_{2h}\right]\hat{\mathbf{E}}=-\left[(\frac{A-2+A^{-1}}{\Delta t^2})+\frac{(c\Delta t)^2}{12}(b_0\hat{L}_{2h})\right]\hat{\mathbf{P}}, \tag{68a}$$

$$\left[(\frac{A-2+A^{-1}}{\Delta t^2})(1+\frac{b_0\Delta t^2}{12})+b_0\right]\hat{\mathbf{P}}=\left[a_0+\frac{a_0\Delta t^2}{12}\frac{(A-2+A^{-1})}{\Delta t^2}\right]\hat{\mathbf{E}}, \tag{68b}$$

where

$$\hat{\mathcal{L}}_h(\mathbf{k})\overset{\text{def}}{=}c^2\hat{L}_{4h}(\mathbf{k})-c^4\frac{\Delta t^2}{12}\left[\hat{L}_{2h}(\mathbf{k})\right]^2. \tag{69}$$

Here,

$$\hat{L}_{4h}(\mathbf{k})\overset{\text{def}}{=}-\widehat{\Delta_{4h}}=\sum_{l=1}^{d}\frac{4}{h_l^2}\sin^2(\xi_l/2)\left[1+\frac{1}{3}\sin^2(\xi_l/2)\right],$$

with $\xi_l=k_lh_l\in[-\pi,\pi]$ as before and with $\hat{L}_{2h}(\mathbf{k})$ defined in (53). Seeking nontrivial solutions then leads to a polynomial equation for A:

$$\left[\frac{A-2+A^{-1}}{\Delta t^2}+\hat{\mathcal{L}}_h-\frac{(c\Delta t)^2}{12}\,a_0\hat{L}_{2h}\right]\left[\left(\frac{A-2+A^{-1}}{\Delta t^2}\right)\left(1+\frac{b_0\Delta t^2}{12}\right)+b_0\right]$$
$$+\left[\left(\frac{A-2+A^{-1}}{\Delta t^2}\right)+\frac{(c\Delta t)^2}{12}(b_0\hat{L}_{2h})\right]\left[a_0+\frac{a_0\Delta t^2}{12}\left(\frac{A-2+A^{-1}}{\Delta t^2}\right)\right]=0. \tag{70}$$

As for the second-order accurate scheme, the number of roots for A is the same as the number of roots s to the corresponding analytic dispersion relation, and so there are no spurious roots for A. Furthermore, for well-resolved modes with $\Delta t\to 0$, $c^2\hat{\mathcal{L}}_h\Delta t^2\to 0$ and $c^2\hat{L}_{2h}\Delta t^2\to 0$, it is straightforward to show that solutions of (70) take the form

$$A=1+s\Delta t+\frac{1}{2}(s\Delta t)^2+\frac{1}{3!}(s\Delta t)^3+\frac{1}{4!}(s\Delta t)^4+\mathcal{O}(\Delta t^5), \tag{71}$$

where s is a root of the corresponding continuous dispersion relation (20). This confirms that the scheme is fourth-order accurate, as expected, since we expect A to be an approximation to $e^{s\Delta t}$.

To analyze the roots of (70), it is useful to use the substitution in (57), which again leads to a quadratic equation in R:

$$R^2-2BR+C=0,$$

where for the fourth-order case the coefficients in the quadratic are now given by

$$B=\frac{\Delta t^2\left(a_0+b_0+\left(1+\frac{b_0\Delta t^2}{12}\right)\hat{\mathcal{L}}_h+\frac{(c\Delta t)^2}{12}\,a_0\hat{L}_{2h}\right)}{8\left(1+\frac{b_0\Delta t^2}{12}+\frac{a_0\Delta t^2}{12}\right)},$$

$$C=\frac{b_0\Delta t^4\hat{\mathcal{L}}_h}{16\left(1+\frac{b_0\Delta t^2}{12}+\frac{a_0\Delta t^2}{12}\right)}.$$

Note that $B^2-C\geqslant 0$ as was the case for the second-order accurate scheme, and thus a sufficient condition for stability is $2B < 1$, or equivalently

$$\frac{\Delta t^2\left(a_0+b_0+\left(1+\frac{b_0\Delta t^2}{12}\right)\hat{\mathcal{L}}_h+\frac{(c\Delta t)^2}{12}a_0\hat{L}_{2h}\right)}{4\left(1+\frac{b_0\Delta t^2}{12}+\frac{a_0\Delta t^2}{12}\right)} < 1. \tag{72}$$

Using the assumption that $c\Delta t/h_l \leqslant 1$ leads to $(c\Delta t)^2\hat{L}_{2h}(\mathbf{k}) = \mathcal{O}(1)$, and thus

$$\Delta t^2\hat{\mathcal{L}}_h(\mathbf{k}) < 4 - K\Delta t^2, \tag{73}$$

for $K = \mathcal{O}(1) > 0$ as $\Delta t \to 0$. Using the definition of $\hat{\mathcal{L}}_h$ in (69) yields

$$\hat{\mathcal{L}}_h(\mathbf{k}) = c^2\sum_{l=1}^{d}\left\{\frac{4}{h_l^2}\sin^2(\xi_l/2)\left(1+\frac{1}{3}\sin^2(\xi_l/2)\right)\right\} - c^2\frac{(c\Delta t)^2}{12}\left[\sum_{l=1}^{d}\frac{4}{h_l^2}\sin^2(\xi_l/2)\right]^2.$$

Assuming $c\Delta t/h_l \leqslant 1$, it can be shown that the maximum of $\hat{\mathcal{L}}_h(\mathbf{k})$ occurs when $\xi_l = \pm\pi$ for all l, so that

$$\max_{|\xi_l|\leqslant\pi}\Delta t^2\hat{\mathcal{L}}_h(\mathbf{k}) = \frac{4}{3}\sum_{l=1}^{d}\frac{4(c\Delta t)^2}{h_l^2} - \frac{1}{12}\left[\sum_{l=1}^{d}\frac{4(c\Delta t)^2}{h_l^2}\right]^2. \tag{74}$$

Finally, setting $Z = \sum_{l=1}^{d}\frac{4(c\Delta t)^2}{h_l^2}$ in (74) and substituting into (73) implies

$$-\frac{1}{12}(Z-4)(Z-12) < -K\Delta t^2,$$

which is true provided $Z < 4 - (3/2)K\Delta t^2$. Therefore, the leading-order time-step stability constraint for the fourth-order scheme is

$$(c\Delta t)^2\sum_{l=1}^{d}\frac{1}{h_l^2} < 1 - \frac{3}{8}K\Delta t^2, \tag{75}$$

which for sufficiently fine grids is essentially the same time-step restriction as for the non-dispersive case. This result is summarized in the following theorem.

Theorem 3. *The fourth-order accurate ADE-GDM scheme for one polarization vector ($N_p = 1$) and zero damping coefficients ($a_1 = b_1 = 0$), and with non-negative values for a_0 and b_0 is neutrally stable provided*

$$\Delta t < \frac{C_{\text{cfl}}}{\sqrt{c^2\sum_{l=1}^{d}\frac{1}{h_l^2}}}, \tag{76}$$

where $C_{\text{cfl}} = 1 - \mathcal{O}(\Delta t^2)$.

The analysis shows that the fourth-order scheme has essentially the same time-step restriction as the second-order accurate scheme.

5.3. Numerical investigation of stability for ADE-GDM

Having investigated the stability of the ADE-GDM schemes analytically for the zero damping case, the purpose of this section is to verify the analysis and also to probe the behaviour of the schemes for nonzero values of the damping parameters, a_1 and b_1, using a numerical evaluation of the roots of the stability polynomials (again assuming $N_p = 1$). Results for both the second- and fourth-order accurate schemes are given. It is shown that the schemes exhibit no growth for parameter values for which the exact solution of the governing equations does not grow, i.e. when the algebraic condition in (22) is satisfied, and when a CFL stability condition holds (as in the theorems above).

For the second-order scheme with $N_p = 1$, the amplification factor satisfies the constraint

$$P(A) \overset{\text{def}}{=} \Big[\big(A - 2 + A^{-1}\big) + c^2\Delta t^2 \hat{L}_{2h}(\mathbf{k})\Big]\Big[\big(A - 2 + A^{-1}\big) + \frac{b_1\Delta t}{2}\big(A - A^{-1}\big) + b_0\Delta t^2\Big] \\ + \big(A - 2 + A^{-1}\big)\Big[\frac{a_1\Delta t}{2}\big(A - A^{-1}\big) + a_0\Delta t^2\Big] = 0, \tag{77}$$

where $\hat{L}_{2h}(\mathbf{k})$ was defined previously in (53). The constraint in (77) is a generalization of the one in (56) for the case of nonzero damping parameters. Multiplication of (77) by A^2 yields a polynomial in A of degree four, and the corresponding four roots of this polynomial can be regarded as functions of $\boldsymbol{\xi} \in [-\pi, \pi]^d$, where $\xi_l = k_l h_l$, the set of model parameters $\vartheta \overset{\text{def}}{=} \{a_0, a_1, b_0, b_1\}$, the time-step Δt, and the CFL parameter

$$\Lambda \overset{\text{def}}{=} \sqrt{c^2\Delta t^2 \sum_{l=1}^{d} \frac{1}{h_l^2}}.$$

Denote by $\mathbf{A}_2(\vartheta, \Delta t, \Lambda)$, the maximum over $\boldsymbol{\xi}$ of the largest $|A|$,

$$\mathbf{A}_2(\vartheta, \Delta t, \Lambda) \overset{\text{def}}{=} \max_{\boldsymbol{\xi}\in[-\pi,\pi]^d,\, P(A)=0} |A|,$$

and let $\Lambda_{\max}(\vartheta, \Delta t)$ be defined to be the largest value of the CFL parameter Λ such that the scheme is “stable”[6], $\mathbf{A}_2 \leqslant 1$, for all $0 < \Lambda(\vartheta, \Delta t) \leqslant \Lambda_{\max}(\vartheta, \Delta t)$. Thus, $\Lambda_{\max}(\vartheta, \Delta t)$ determines the maximum stable time-step for a given set of parameters. Due to the large number of parameters, it is difficult to show the full behaviour of $\Lambda_{\max}(\vartheta, \Delta t)$. For clarity, therefore, a selection of parameters are chosen to have some fixed values while others are allowed to vary over some range. We note that due to roundoff errors in the numerical computations, the stability condition is taken to be $\mathbf{A}_2 \leqslant 1 + \epsilon$, with $\epsilon = 10^{-6}$ for the second-order accurate scheme and $\epsilon = 10^{-5}$ for the fourth-order accurate scheme.

Figure 2 shows contours of $\Lambda_{\max}$ for the second-order accurate scheme. The three plots in the top row show contours of $\Lambda_{\max}$ as a function of $a_0 \in [0, 1]$ and $b_0 \in [0, 1]$ for $a_1 = b_1 = 0$ and $\Delta t = 1$, 0.5 and 0.25. These plots show that the scheme is stable with a value of $\Lambda_{\max}$ close to 1 in agreement with the stability analysis of Section 5.1. There is some dependence of $\Lambda_{\max}$ on a_0

---

[6] For the purposes of the discussion here, “stable” is defined to be no growth in the solution. In general one may allow bounded growth in the solution; this would be the appropriate definition when the true solution exhibits growth. It practice the schemes defined here are found to converge at the expected order of accuracy even when the true solution grows.

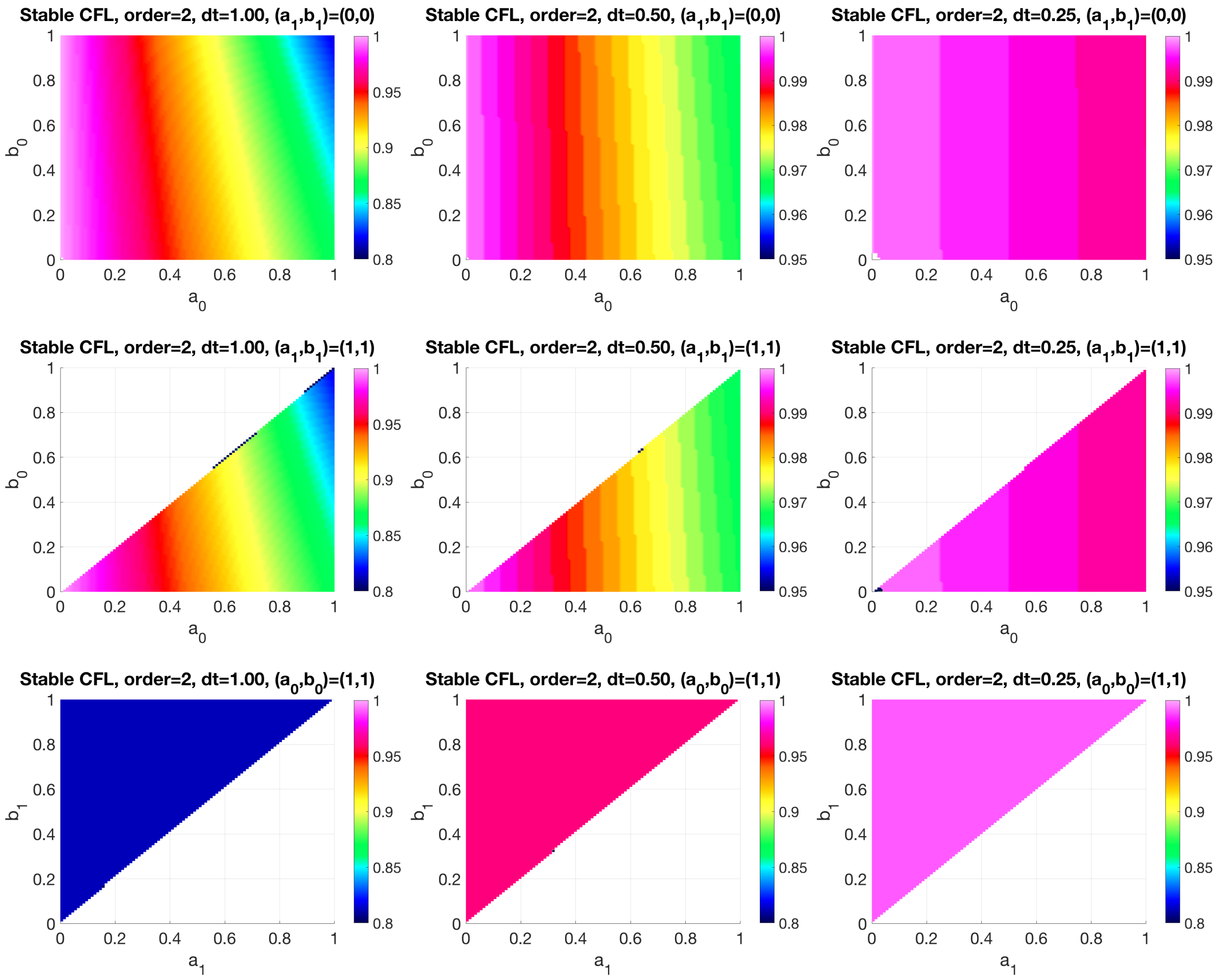

Figure 2: Stability bound for the second-order accurate scheme. The maximum stable CFL number is shown as a function of the GDM parameters. No values are shown where the numerical solution shows growth and this closely matches the regions where the true solution shows growth, $a_0\, b_1 < a_1\, b_0$.

and b_0, especially for larger values of a_0, b_0 and Δt, as expected from the stability bound in (66). The three plots in the middle row of Figure 2 show similar contours but for $a_1 = 1$ and $b_1 = 1$. No contours are plotted where $\Lambda_{\max} = 0$; this corresponds to regions where the numerical solution has growth in time. As seen in the figure, the scheme is found to have no growth when $a_1 b_0 < a_0 b_1$, but to have growth otherwise. This agrees with (22) that specifies when the analytic solution does not grow. The bottom three contours fix $a_0 = b_0 = 1$ and vary $a_1 \in [0, 1]$ and $b_1 \in [0, 1]$. These results also demonstrate that the numerical scheme has no growth for $a_1 b_0 < a_0 b_1$.

A similar investigation is performed for the fourth-order accurate scheme with corresponding amplification factor $\mathbf{A}_4$. The results are shown in Figure 3 and show an overall behaviour that is similar to the second-order accurate scheme. Without damping, as seen in the top three contours, the scheme has a stability bound near 1 as a_0 and b_0 are varied. With damping, as seen in the plots in the middle and bottom rows, the scheme has no growth in the region $a_1 b_0 < a_0 b_1$.

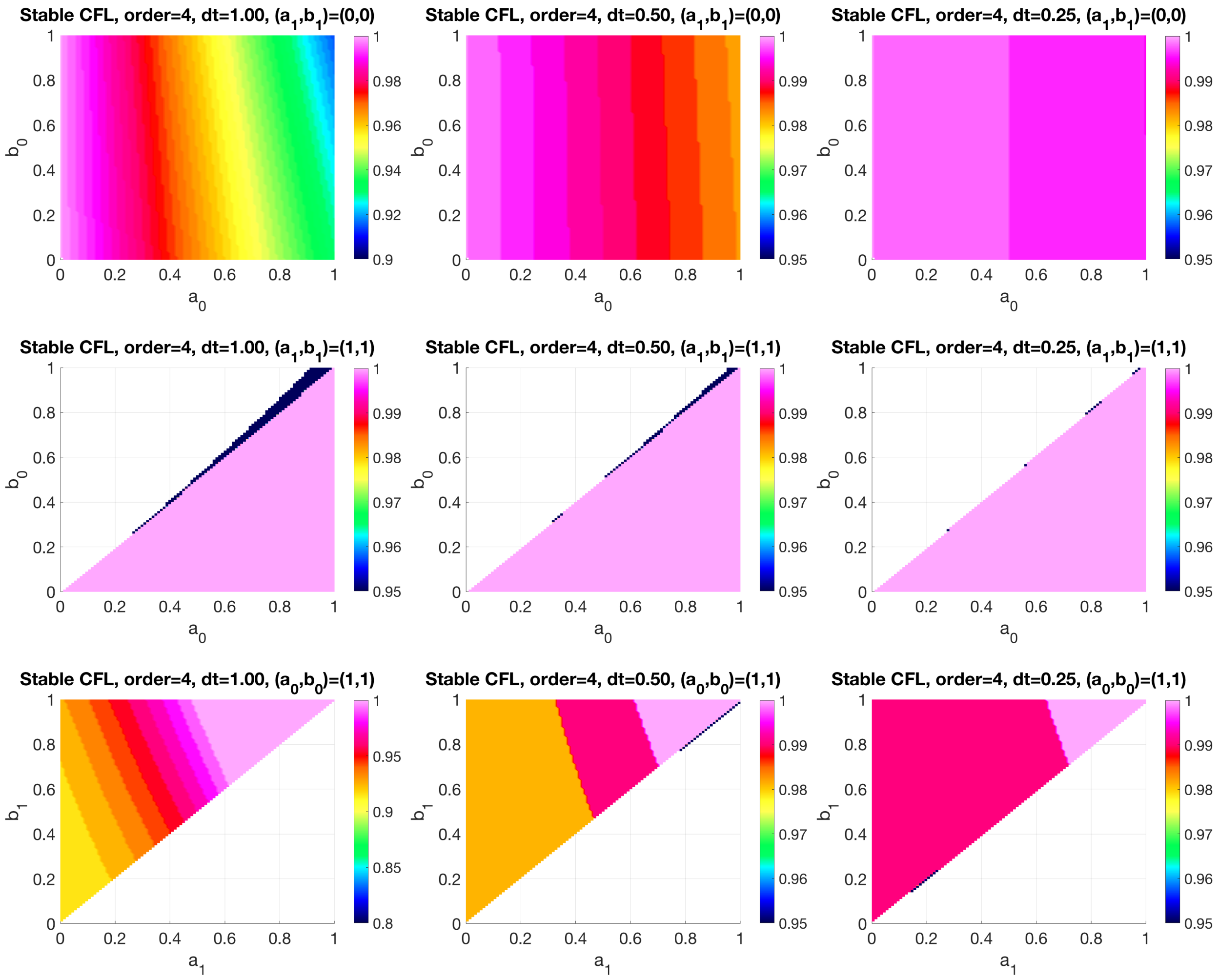

Figure 3: Stability bound for the fourth-order accurate scheme. The maximum stable CFL number is shown as a function of the GDM parameters. No values are shown where the numerical solution shows growth and this closely matches the regions where the true solution shows growth, $a_0\, b_1 < a_1\, b_0$.

6. Numerical results

In this section, numerical results are presented to verify the implementation, stability and numerical convergence of the ADE-GDM scheme for the dispersive Maxwell's equations in second-order form on overlapping grids. A variety of different configurations are considered, and grid refinement studies are performed to assess the accuracy of the solution as the mesh is refined. Problems are selected to demonstrate the properties of the numerical scheme, as well as the use of overlapping grids to accommodate non-rectangular geometries in both two and three dimensions. In addition, we include several standard dispersion tests with the classical Drude material model (a special case of the GDM model) and PEC boundary conditions to facilitate comparison with other schemes. Before presenting the numerical results, Section 6.1 discusses the general procedure for deriving exact solutions of the GDM model, which are used to in the convergence studies.

The first problem considered in Section 6.2 is the propagation of a dispersive plane wave. This simple configuration is a good benchmark for future comparisons to other schemes. In Section 6.3, the GDM eigenmodes for a square and box domains are computed. This example involves simple geometrical configurations that includes physical PEC boundary conditions. In Section 6.4, the eigenmodes for a two-dimensional disk and three-dimensional cylinder are computed. This example demonstrates the accuracy of the schemes for overlapping grids with curved PEC boundaries. Section 6.5 considers the scattering of a dispersive plane-wave from a PEC cylinder in two dimensions and a PEC sphere in three dimensions. These last two examples generalize the classical Mie-series exact-solutions to the case of GDM materials.

All numerical studies are performed with the Overture-based **CgMx** solver[7], to which the second- and fourth-order accurate schemes presented in Section 3 have been added. Overture provides tools to generate high-quality composite grids for high-order methods along with a suite of PDE solvers for various problems in computational physics (compressible and incompressible flows, solid mechanics, conjugate heat transfer, electrodynamics, etc). Overture's overlapping structured grid generator **Ogen** is used to create all of the composite grids (see Section 4.1), and the **CgMx** solver is used to compute all the solutions.

6.1. Exact separable solutions for the GDM model

A number of the exact solutions that are used to verify the ADE-GDM scheme in the subsequent sections are generalized from the non-dispersive case. The extension of the non-dispersive solutions to the case of a GDM model requires a number of modifications to the usual construction. This section briefly outlines these modifications.

The exact solutions under consideration take the form of separable solutions in t and $\mathbf{x}$ with an exponential time dependence,

$$\mathbf{E}(\mathbf{x},t) = e^{st}\,\hat{\mathbf{E}}(\mathbf{x}), \qquad \mathbf{H}(\mathbf{x},t) = e^{st}\,\hat{\mathbf{H}}(\mathbf{x}), \qquad \mathbf{P}_m(\mathbf{x},t) = e^{st}\,\hat{\mathbf{P}}_m(\mathbf{x}).$$

Substituting this ansatz into (2b) (essentially a Laplace transform in time but ignoring initial conditions) leads to the relation (10) between the polarization vectors and $\mathbf{E}$. The wave equations (2a) and (3) for the electric and magnetic fields, $\mathbf{E}$ and $\mathbf{H}$, respectively, then transform to the vector Helmholtz equations

$$\Delta\hat{\mathbf{E}} = \eta(s)\hat{\mathbf{E}}, \tag{78a}$$

$$\Delta\hat{\mathbf{H}} = \eta(s)\,\hat{\mathbf{H}}, \tag{78b}$$

where

$$\eta(s) \overset{\text{def}}{=} \frac{s^2}{c^2}(1+\hat{\chi}(s)), \tag{78c}$$

with $\hat{\chi}(s)$ given in (7). From the first-order form in (1), $\hat{\mathbf{E}}$ and $\hat{\mathbf{H}}$ are related by

$$\hat{\mathbf{H}} = -\frac{1}{\mu s}\nabla\times\hat{\mathbf{E}}, \tag{79a}$$

$$\hat{\mathbf{E}} = \frac{s\mu_0}{\eta(s)}\,\nabla\times\hat{\mathbf{H}}, \tag{79b}$$

---

[7] See `www.overtureFramework.org` for documentation, run scripts and software downloads.

which can be used to compute $\hat{\mathbf{H}}$ given $\hat{\mathbf{E}}$, or $\hat{\mathbf{E}}$ given $\hat{\mathbf{H}}$. Note that the non-dispersive case corresponds to the case $\hat{\chi}(s) = 0$ in (78c), and so for time periodic solutions with $s = -i\omega$, it is clear that $\eta = -(c/\omega)^2 = -k^2$. The primary change moving to the dispersive case is that the parameters s and $\eta(s)$ can be complex, in general, and so dispersive solutions can decay (or grow) in time and/or space.

It can be seen from (78a) and (78b) that in the dispersive case, $\hat{\mathbf{E}}$ and $\hat{\mathbf{H}}$ satisfy vector Helmholtz equations, similar to the non-dispersive case. For a given problem, these equations are augmented by appropriate boundary conditions. Thus, the spatial form of solutions to eigenvalue problems (e.g. eigenmodes for a square, box, disk or cylinder) or to scattering problems (e.g. scattering from a PEC cylinder or sphere) have a similar spatial form to the non-dispersive case although the form of the temporal evolution may allow growth or decay since η can in general be complex. Note that all computations presented here are performed using real arithmetic. The real part of the exact solutions are obtained by first deriving the full complex-valued solution, and then retaining only the real part as the exact solution.

The precise form of the exact solution hinges on the dispersion relation (11), which in turn depends on the specifics of the GDM model. For the computations presented in subsequent sections, we take[8] $\epsilon_0 = 1$ and $\mu_0 = 1$, and use sets of GDM parameters for either 1 or 2 polarization vectors as given in Table 1. The parameter set denoted by $\mathcal{S}_{\text{ND}}$ ("no-damping") has a single polarization vector and is an undamped dispersive material. Set $\mathcal{S}_{\text{D}}$ ("Drude") has a single polarization vector and corresponds to the classical Drude material model. Note that in terms of traditional parameters defining the Drude model, a_0 corresponds to ω_p^2 while b_1 corresponds to γ. Finally, set $\mathcal{S}_{\text{GDM}}$ has two polarization vectors with all terms in the GDM model present for both. The corresponding roots s of the dispersion relation (11) are given below for each numerical example. Note that in all two-dimensional computations presented, the transverse electric (TE-z) mode (E_x, E_y, H_z) is considered.

GDM Parameters for simulations					
set	N_p	$a_{0,m}$	$a_{1,m}$	$b_{0,m}$	$b_{1,m}$
$\mathcal{S}_{\text{ND}}$	1	0.9	0	1	0
$\mathcal{S}_{\text{D}}$	1	1	0	0	.9
$\mathcal{S}_{\text{GDM}}$	2	0.9 , 0.7	0.2 , 0.1	1 , 2	0.5 , 0.3

Table 1: Sets $\mathcal{S}_{\text{ND}}$, $\mathcal{S}_{\text{GDM}}$, and $\mathcal{S}_{\text{D}}$ of GDM parameters used in the numerical simulations.

6.2. GDM plane wave solution

Consider exact traveling wave solutions to Maxwell's equations with the GDM model of the form

$$\mathbf{E}(\mathbf{x},t) = e^{st} e^{i\mathbf{k}\cdot\mathbf{x}}\,\hat{\mathbf{E}},$$
$$\mathbf{P}_m(\mathbf{x},t) = e^{st} e^{i\mathbf{k}\cdot\mathbf{x}}\,\hat{\mathbf{P}}_m, \qquad m = 1, 2, \ldots, N_p,$$

where s and $k \overset{\text{def}}{=} |\mathbf{k}|$ satisfy the dispersion relation (11). For this test, the computational domain is taken to be the unit square, $\Omega = [0,1]^2$, or unit cube, $\Omega = [0,1]^3$, and the domain is discretized

---

[8] We have non-dimensionalized the problem by an appropriate length and time scale so that $c = 1$.

using a uniform Cartesian grid. The boundary conditions are set using the exact traveling-wave solution. Specific solutions are defined by fixing the wave-vector $\mathbf{k}$ and then numerically determining roots of (11), for example by computing the eigenvalues of the associated companion matrix. For the results presented here, $\mathbf{k} = [4\pi, 4\pi]$ for two dimensions, while in three dimensions we set $\mathbf{k} = [4\pi, 4\pi, 0]$. Note that these particular wave vectors are chosen for convenience of presentation, and other choices yield similar results. Also note that for the cases run here, $\hat{\mathbf{E}} = [1, -1, 1]^T$ with $\hat{\mathbf{P}}_m$ then determined using (10). With these choices, the divergence constraint is satisfied since $\mathbf{k} \cdot \hat{\mathbf{E}} = 0$.

Roots of the dispersion relation for a plane wave		
Set	$\mathcal{S}_{\text{ND}}$	$\mathcal{S}_{\text{GDM}}$
ck	$4\sqrt{2}\pi$	$4\sqrt{2}\pi$
s_R	$0.9985737152943i$	$-0.2490458903963 + 0.9671824116021i$
s_N	$17.79691522062i$	$-0.1515848220324 + 17.81237691252i$

Table 2: Roots of the dispersion relation for the plane wave solution with GDM parameters corresponding to material sets $\mathcal{S}_{\text{ND}}$ and $\mathcal{S}_{\text{GDM}}$, as given in Table 1.

2D plane wave, resonant mode, $\mathcal{S}_{\text{ND}}$				
h_j	$\mathbf{E}$	r	$\mathbf{P}$	r
1/10	1.3e-2		1.0e-3	
1/20	2.9e-4	44.1	2.5e-5	41.5
1/40	2.1e-5	13.4	1.5e-6	17.0
1/80	1.4e-6	15.2	9.3e-8	16.0
1/160	8.8e-8	15.9	5.9e-9	15.7
rate	4.19		4.30	

2D plane wave, non-resonant, $\mathcal{S}_{\text{ND}}$				
h_j	$\mathbf{E}$	r	$\mathbf{P}$	r
1/10	5.6e-2		2.6e-4	
1/20	1.6e-3	34.0	1.7e-5	15.7
1/40	1.1e-4	15.4	1.0e-6	16.3
1/80	6.5e-6	16.4	6.3e-8	16.3
1/160	4.0e-7	16.1	3.9e-9	16.1
rate	4.21		4.01	

3D plane wave, resonant mode, $\mathcal{S}_{\text{ND}}$				
h_j	$\mathbf{E}$	r	$\mathbf{P}$	r
1/10	2.5e-2		1.3e-3	
1/20	1.1e-3	21.8	6.5e-5	20.5
1/40	6.1e-5	18.4	3.6e-6	17.8
1/80	3.5e-6	17.3	2.1e-7	17.4
1/160	2.2e-7	16.0	1.3e-8	16.3
rate	4.18		4.16	

3D plane wave, non-resonant, $\mathcal{S}_{\text{ND}}$				
h_j	$\mathbf{E}$	r	$\mathbf{P}$	r
1/10	1.4e-1		3.1e-4	
1/20	8.2e-3	17.4	2.1e-5	14.7
1/40	5.0e-4	16.2	1.3e-6	16.4
1/80	3.0e-5	16.9	7.9e-8	16.3
1/160	1.8e-6	16.1	4.9e-9	16.0
rate	4.06		4.00	

Figure 4: Max-norm convergence results for a dispersive plane wave in 2D and 3D for parameter set $\mathcal{S}_{\text{ND}}$ and using the fourth-order accurate scheme with $C_{\text{cfl}} = 0.95$. At left are results for resonant modes, while at right are results for non-resonant modes. The column labeled "r" denotes the ratio of the error at the current resolution to the error at the previous resolution. A least squares estimate of the convergence rate over the entire range of grid refinements is also given.

Table 2 shows the specific roots to the dispersion relation for which numerical results are presented. These specific roots have been selected as representative resonant and non-resonant modes, as discussed in Section 2.2, and are referred to as mode "R" and "N", respectively. The notion of resonance indicates that the dispersive effects of the GDM model are significant with respect to the wave motion of the non-dispersive Maxwell's equations. Therefore in the present example with $ck = 4\sqrt{2}\pi \approx 17.8$, non-resonant modes have the magnitude of the imaginary part of s, $|\Im(s)|$, near that value, whereas resonant modes have $|\Im(s)|$ significantly modified by the dispersion in the model. For example, $s_R \approx 1.00i$ is considered resonant for parameter set $\mathcal{S}_{\rm ND}$ in Table 2, while $s_N \approx 17.80i$ is considered non-resonant. More generally, non-resonant modes have the largest imaginary part in magnitude (corresponding to fast propagation with respect to a vacuum), while resonant modes have significantly smaller imaginary component (corresponding to a significant alteration of the wave speed).

Computational results for resonant and non-resonant cases are presented in Figure 4, which show maximum norm errors and estimated convergence rates for the electrical field $\mathbf{E}$ and the polarization $\mathbf{P}$ at $t = 0.5$ computed using the fourth-order accurate scheme with $C_{\rm cfl} = 0.95$[9]. These results demonstrate that the scheme converges with the designed accuracy for both resonant and non-resonant modes.

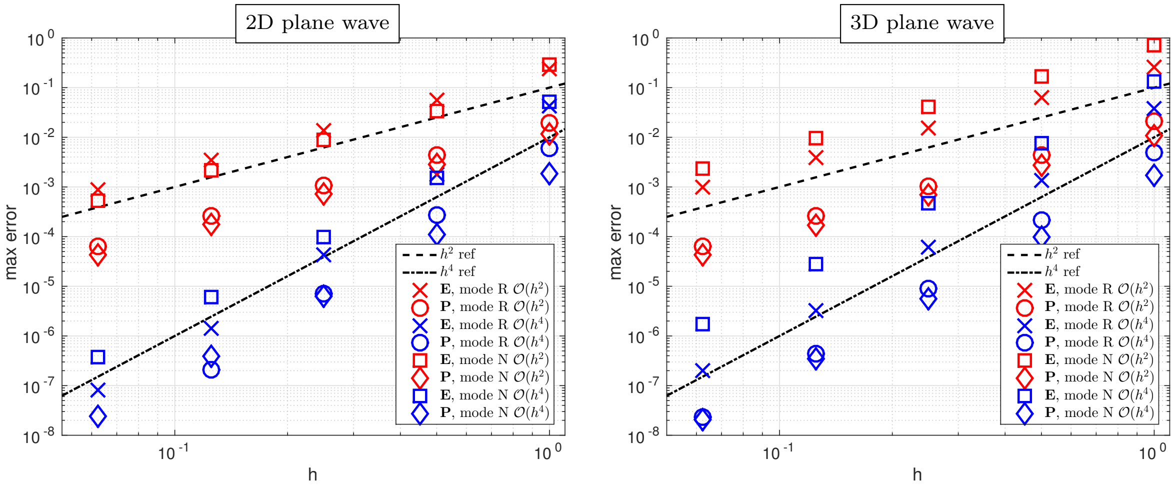

Figure 5: Convergence study for $\|\mathbf{E}\|_\infty$ and $\|\mathbf{P}\|_\infty$ for the exact plane wave solution with parameter set $\mathcal{S}_{\rm GDM}$ using the second- and fourth-order accurate schemes in 2D (left) and 3D (right) on a rectangular grid. In all cases, mode R corresponds to a resonant wave, and mode N corresponds to a non-resonant wave.

Given the large number of potential cases (parameter sets, dimensionality, resonance, and order of scheme), results will subsequently be presented in a graphical manner in an effort to show all results compactly. For example, results for parameter set $\mathcal{S}_{\rm GDM}$ at $t = 0.5$ are shown in Figure 5, which presents the max-norm errors versus grid size on a log-log plot for $d = 2$ and 3, and using both the second- and fourth-order accurate discretizations. Reference lines indicating the expected convergence rates for the respective schemes are also shown. In all cases, the ADE-GDM scheme is shown to converge at or near the designed rate.

6.3. Eigenmodes of a PEC square and box

Now consider computing the eigenmodes of a two-dimensional square and three-dimensional box with PEC boundaries. We start with a standard benchmark test using a classical Drude material (a special case of the GDM model), and then proceed with a general GDM material including multiple polarization vectors. As discussed in Section 6.1, the exact solutions for this case are

---

[9] The choice here to run at $C_{\rm cfl} = 0.95$, instead of the value $C_{\rm cfl} = 0.9$ used elsewhere, was made to avoid a fortuitous super-convergence for the fourth-order scheme with the resonant model caused by a cancellation in truncation error terms at $C_{\rm cfl} = 0.9$.

of a similar form to the well-known exact solutions for the case of a non-dispersive material. In particular, each component of the electric field satisfies a Helmholtz equation (78a) with either Dirichlet or Neumann boundary conditions. For example, in a box $\mathcal{B} = [0, L_x] \times [0, L_y] \times [0, L_z]$, the x-component of the electric field is

$$E_x(\mathbf{x}, t) = C_x \cos\left(\frac{\alpha_1\,\pi x}{L_x}\right) \sin\left(\frac{\alpha_2\,\pi y}{L_y}\right) \sin\left(\frac{\alpha_3\,\pi z}{L_z}\right) e^{s_{\boldsymbol{\alpha}} t}, \tag{80}$$

for any integer values of the d components of the multi-index $\boldsymbol{\alpha} = (\alpha_1, \ldots, \alpha_d)$. Here, $s_{\boldsymbol{\alpha}}$ is a root of equation

$$\eta(s) = \frac{s^2}{c^2}(1 + \hat{\chi}(s)) = -\lambda_{\boldsymbol{\alpha}}^2, \tag{81}$$

where $\hat{\chi}(s)$ is defined in (7a) and

$$\lambda_{\boldsymbol{\alpha}}^2 = \left(\frac{\alpha_1\,\pi}{L_x}\right)^2 + \left(\frac{\alpha_2\,\pi}{L_y}\right)^2 + \left(\frac{\alpha_3\,\pi}{L_z}\right)^2. \tag{82}$$

The computations presented in this work use $\boldsymbol{\alpha} = (4, 4)$ for two space dimensions, and $\boldsymbol{\alpha} = (4, 4, 4)$ for three space dimensions. In both the Drude material $\mathcal{S}_{\text{D}}$ and the general GDM material $\mathcal{S}_{\text{GDM}}$, both resonant and non-resonant modes are considered. Table 3 gives roots of the dispersion relation (81) for the Drude model with material parameters $\mathcal{S}_{\text{D}}$, while Table 4 gives roots of the dispersion relation for the the general GDM material using $\mathcal{S}_{\text{GDM}}$.

Roots of the dispersion relation for eigenmodes of a square or box with $\mathcal{S}_{\text{D}}$		
	$2D$ square	$3D$ box
$\boldsymbol{\alpha}$	$(4, 4)$	$(4, 4, 4)$
s_R	$-.8971665345572$	$-.8981074450078$
s_N	$-.001416732721401 + 1.779957293694i$	$-.0009462774961050 + 21.78851327280i$

Table 3: Roots of the GDM dispersion relation for eigenfunctions of a square and box with PEC boundaries, and material corresponding to parameter set $\mathcal{S}_{\text{D}}$ (a Drude material) as given in Table 1.

Roots of the dispersion relation for eigenmodes of a square or box with $\mathcal{S}_{\text{GDM}}$		
	$2D$ square	$3D$ box
$\boldsymbol{\alpha}$	$(4, 4)$	$(4, 4, 4)$
s_R	$-0.2490458903963 + 0.9671824116021i$	$-0.2493648636708 + 0.9675370281513i$
s_N	$-0.1515848220324 + 17.81237691252i$	$-0.1510565353711 + 21.79890966705i$

Table 4: Roots of the GDM dispersion relation for eigenfunctions of a square and box with PEC boundaries, and material corresponding to parameter set $\mathcal{S}_{\text{GDM}}$ as given in Table 1.

Computational convergence studies are performed for the eigenmodes of a square with $L_x = L_y = 1$, and box with $L_x = L_y = L_z = 1$ using uniform Cartesian grids and $C_{\text{cfl}} = 0.9$. A representative computation is depicted in Figure 6, which shows the x-component of the electric field E_x, the error in E_x, and the y-component of the first polarization vector at $t = 1.0$ for the resonant mode from Table 4, as computed on a square using the fourth-order accurate ADE-GDM scheme. Of particular note is the smoothness of the error in the electric field for this fourth-order case, even up to the boundary. A more comprehensive set of convergence results at $t = 0.7$ using the max-norm are shown in Figure 7 for material parameter set $\mathcal{S}_{\rm D}$ and in Figure 8 for material parameters $\mathcal{S}_{\rm GDM}$. These figures illustrate that the schemes converge at or near their designed rate for $\mathbf{E}$ and $\mathbf{P}$ for all cases.

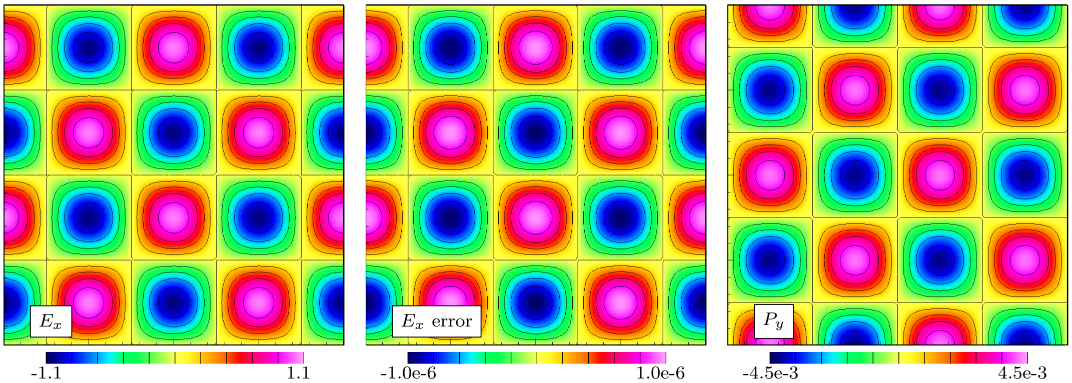

Figure 6: GDM eigemode of a square with PEC BCs on grid with grid-spacing $h = 1/128$ at $t = 1$ computed with the fourth-order accurate ADE-GDM scheme and $C_{\rm cfl} = 0.9$. Left: E_x. Middle: error in E_x. Right: P_y.

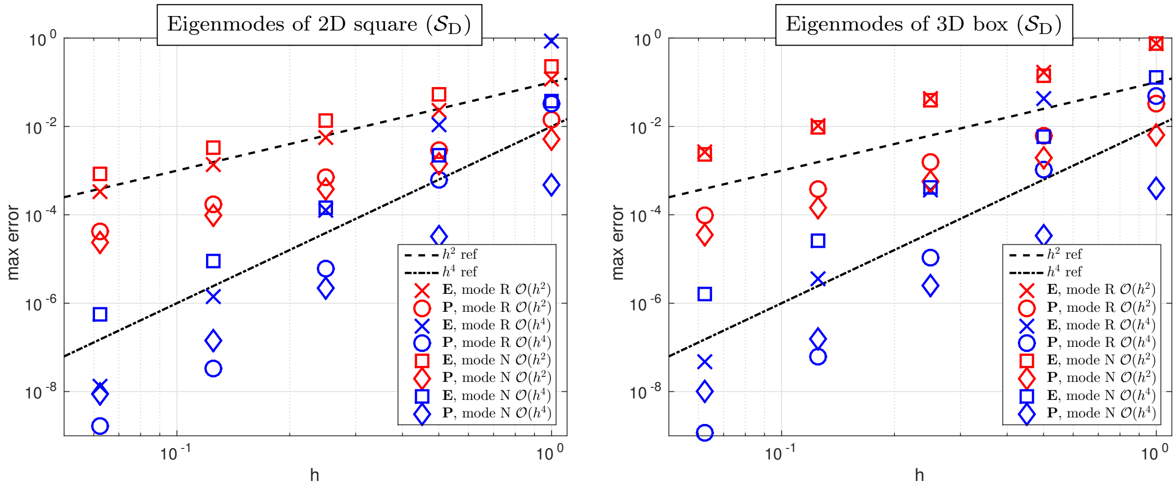

Figure 7: Convergence study in $\|\mathbf{E}\|_\infty$ and $\|\mathbf{P}\|_\infty$ for the eigenmodes of a two-dimensional PEC square (left), and a three-dimensional PEC box (right) using the second- and fourth-order accurate schemes. All computations use the $\mathcal{S}_{\rm D}$ parameter set from Table 1, with corresponding resonant and non-resonant roots of the dispersion relation given in Table 3.

6.4. *Eigenmodes of a PEC disk and cylinder*

The prior numerical examples have all used a single Cartesian grid on a square or box geometry, with no overlapping-grid construction required. In the present section we consider eigenmode oscillations on a disk in two dimension and a cylinder in three-dimensional space. The TE-z eigenmodes for these geometries, disk and cylinder, with PEC boundary conditions can be determined for the

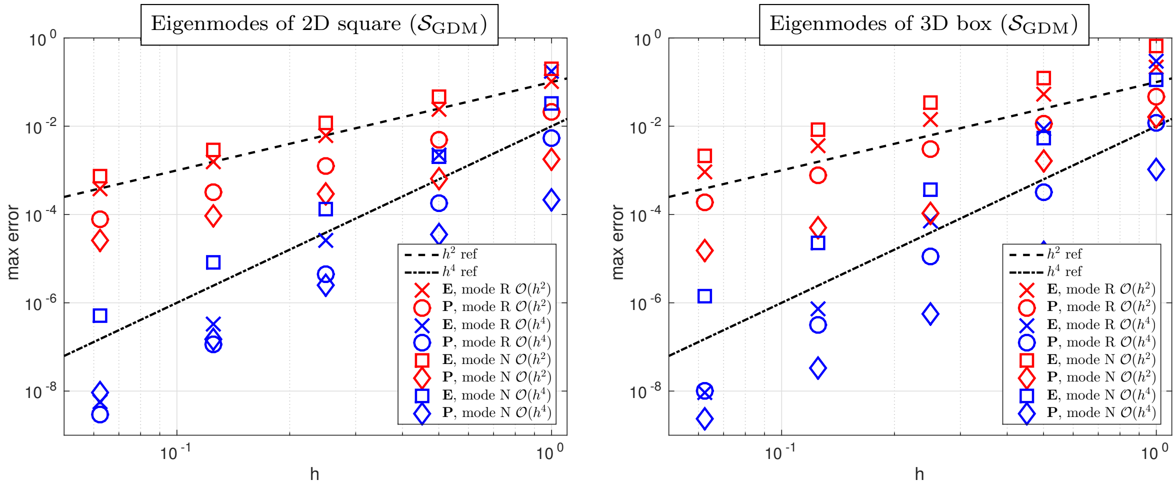

Figure 8: Convergence study in $\|\mathbf{E}\|_\infty$ and $\|\mathbf{P}\|_\infty$ for the eigenmodes of a two-dimensional PEC square (left), and a three-dimensional PEC box (right) using the second- and fourth-order accurate schemes. All computations use the $\mathcal{S}_{\rm GDM}$ parameter set from Table 1, with corresponding resonant and non-resonant roots of the dispersion relation given in Table 4.

GDM-ADE equations in a similar manner to the non-dispersive case. As in the non-dispersive case, we find the eigenvalues and eigenmodes to the boundary value problem

$$\Delta \hat{H}_z = -\lambda_{\boldsymbol{\alpha}}^2 \hat{H}_z, \qquad \mathbf{x} \in \Omega, \tag{83a}$$

$$\frac{\partial \hat{H}_z}{\partial n} = 0, \qquad \mathbf{x} \in \partial\Omega, \tag{83b}$$

where $\lambda_{\boldsymbol{\alpha}} \in \mathbb{R}$ are eigenvalues (of which there are an infinite number). Values for $s_{\boldsymbol{\alpha}}$ are found for a given $\lambda_{\boldsymbol{\alpha}}$ as roots of the equation

$$\eta(s) \overset{\text{def}}{=} \frac{s^2}{c^2}(1 + \hat{\chi}(s)) = -\lambda_{\boldsymbol{\alpha}}^2,$$

and the exact solution for H_z is

$$H_z(\mathbf{x}, t) = \hat{H}_z(\mathbf{x})\, e^{s_{\boldsymbol{\alpha}} t}.$$

The corresponding electric field is then determined from (79b) and $\mathbf{P}_m$ is given by (10). The PEC conditions (46a) on the electric field $\mathbf{E}$ are satisfied by construction.

Overlapping grids for these cases consist of a thin boundary-fitted annular grid and a large background Cartesian grid, see for example Figures 9 and 10. The two-dimensional geometry, as illustrated in Figure 9, has a disk of radius $R = 1$ centered at the origin, and is discretized using an overlapping grid, called $\mathcal{G}^{(2)}$ in the figure, with approximate grid spacing $h \approx 1/20$. The notation $\mathcal{G}^{(j)}$ is meant to be generic, and indicates a grid with approximate grid spacing $h \approx 1/(10j)$, and so grid refinement studies will typically take $j = 1, 2, 4, 8, 16$, for example. The three-dimensional geometry, as shown in Figure 10, is a cylindrical tube of unit length $H = 1$ in the z-direction, with a circular cross section of radius $R = 1$ centered at the origin. The overlapping grid shown in Figure 10 for this geometry is denoted by $\mathcal{G}^{(1)}$, which indicates that the approximate grid spacing in all directions is $h \approx 1/10$. In the computations, the GDM material is taken to be the $\mathcal{S}_2$ parameter set. The exact solution in two dimensions is computed for $\boldsymbol{\alpha} = (2, 2)$, while $\boldsymbol{\alpha} = (1, 1, 1)$ is used for the three-dimensional case, and both resonant and non-resonant modes are considered. The roots of the dispersion relation defining the various exact solutions for all cases is presented in Table 6.

Roots of the dispersion relation for eigenmodes of a disk and cylinder with $\mathcal{S}_{\rm D}$		
	$2D$ disk	$3D$ cylinder
$\boldsymbol{\alpha}$	$(2, 2)$	$(1, 1, 1)$
s_R	$-.8911053445114$	$-.8852147959837$
s_N	$-.004447327744287 + 10.01909890269i$	$-.007392602008164 + 7.750801119295i$

Table 5: GDM roots of the dispersion relation corresponding to the Drude material with $\mathcal{S}_{\rm D}$ parameters from Table 1 for PEC eigenfunctions of a disk and cylinder.

Roots of the dispersion relation for eigenmodes of a disk and cylinder with $\mathcal{S}_{\rm GDM}$		
	$2D$ disk	$3D$ cylinder
$\boldsymbol{\alpha}$	$(2, 2)$	$(1, 1, 1)$
s_R	$-0.2469392239304 + 0.9648621424962i$	$-0.1980569982541 + 0.5085729538910i$
s_N	$-0.1550353933625 + 10.04274371916i$	$-.6104976708475 + 7.690546586525i$

Table 6: GDM roots of the dispersion relation corresponding to set $\mathcal{S}_{\rm GDM}$ of GDM parameters shown in Table 1 for PEC eigenfunctions of a disk and cylinder.

Representative computational results using $C_{\rm cfl} = 0.9$ for the two-dimensional disk are shown in Figure 9, which includes a plot showing a coarse version of the overlapping grid. The figure shows the x-component of the electric field, as computed on $\mathcal{G}^{(16)}$ at $t = 1$. The error in E_x at $t = 1$ is also displayed, which illustrates the smooth and small error in the computed solution. Figure 10 shows analogous results for the cylindrical domain, and again the computation is observed to be very well behaved, with smooth error up to the boundary and through the interpolation interface. Results of convergence studies at $t = 0.7$ with $C_{\rm cfl} = 0.9$ for two- and three-dimensional cases are presented in Figure 11 for the parameter set $\mathcal{S}_{\rm D}$ corresponding to a Drude medium, and Figure 12 for the parameter set $\mathcal{S}_{\rm GDM}$. In these figures, max-norm errors illustrate convergence of the computed solutions at or near the expected rates for both resonant and non-resonant modes.

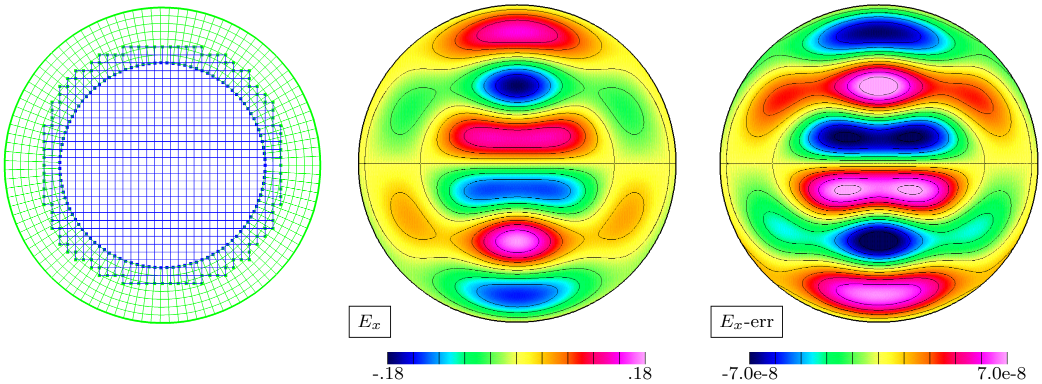

Figure 9: At left a coarse grid representation of the disk $\mathcal{G}^{(2)}$. At center is the E_x field for a GDM eigenmode of a disk with PEC BCs on grid $\mathcal{G}^{(16)}$ at $t = 1$ computed using the fourth-order accurate ADE-GDM scheme with $C_{\rm cfl} = 0.9$, and at right is the error in the computed E_x field.

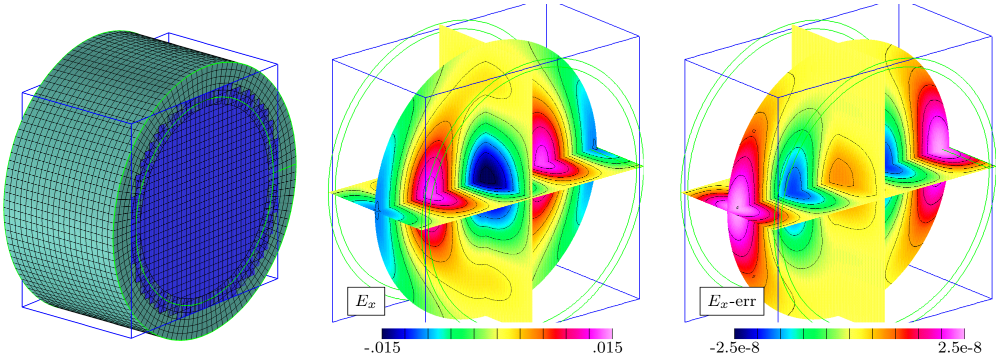

Figure 10: At left a coarse grid representation of the cylinder $\mathcal{G}^{(1)}$. At center is the E_x field for a GDM eigenmode of a cylinder with PEC BCs on grid $\mathcal{G}^{(4)}$ at $t = 1$ computed using the fourth-order accurate ADE-GDM scheme and $C_{\rm cfl} = 0.9$, and at right is the error in the computed E_x field.

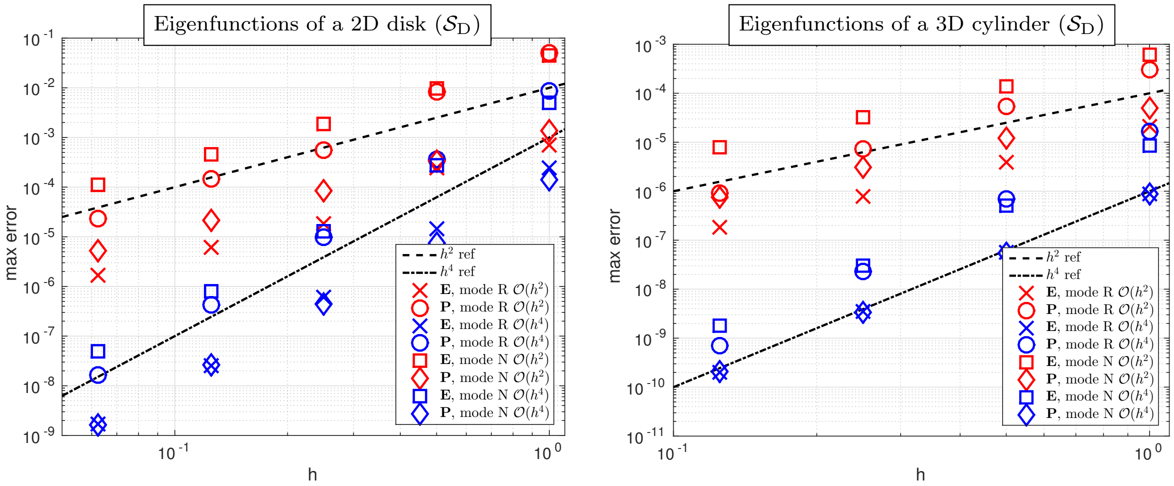

Figure 11: Convergence study in $\|\mathbf{E}\|_\infty$ and $\|\mathbf{P}\|_\infty$ at $t = 0.7$ and $C_{\rm cfl} = 0.9$ for the eigenmodes of a two-dimensional PEC disk (left), and a three-dimensional PEC cylinder (right) using the second- and fourth-order accurate schemes. All computations use the Drude material with $\mathcal{S}_{\rm D}$ parameters from Table 1, with corresponding resonant and non-resonant roots of the dispersion relation given in Table 5.

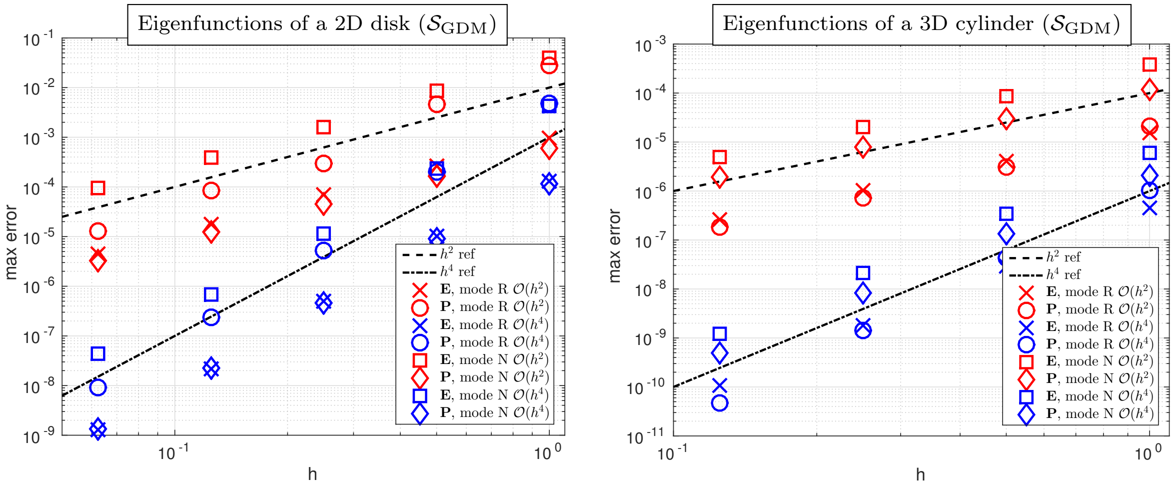

Figure 12: Convergence study in $\|\mathbf{E}\|_\infty$ and $\|\mathbf{P}\|_\infty$ at $t = 0.7$ and $C_{\rm cfl} = 0.9$ for the eigenmodes of a two-dimensional PEC disk (left), and a three-dimensional PEC cylinder (right) using the second- and fourth-order accurate schemes. All computations use the $\mathcal{S}_{\rm GDM}$ parameter set from Table 1, with corresponding resonant and non-resonant roots of the dispersion relation given in Table 6.

6.5. *GDM scattering from a PEC cylinder and a PEC sphere*

In this example we consider the scattering of a dispersive TE-z plane wave from a PEC cylinder in two dimensions and from a PEC sphere in three dimensions. The solution of the dispersive model is determined analytically following the same steps as the classical solution for non-dispersive electromagnetics. The key is to solve a scalar Helmholtz boundary-value problem for scattered field $\hat{H}_z^s$,

$$\Delta \hat{H}_z^s = \eta(s)\, \hat{H}_z^s, \tag{84}$$

with appropriate boundary conditions (the classical Mie series solution) in terms of Bessel functions. Given the solution for $\hat{H}_z^s$, the electric field $\mathbf{E}$ is found from (79b) while the polarization $\mathbf{P}_m$ is determined from (10). Depending on the choice of s or $\eta(s)$, the solution may decay in space or time. We take $\eta = -k^2$, $k \in \mathbb{R}$, and solve for s from the dispersion relation (11).

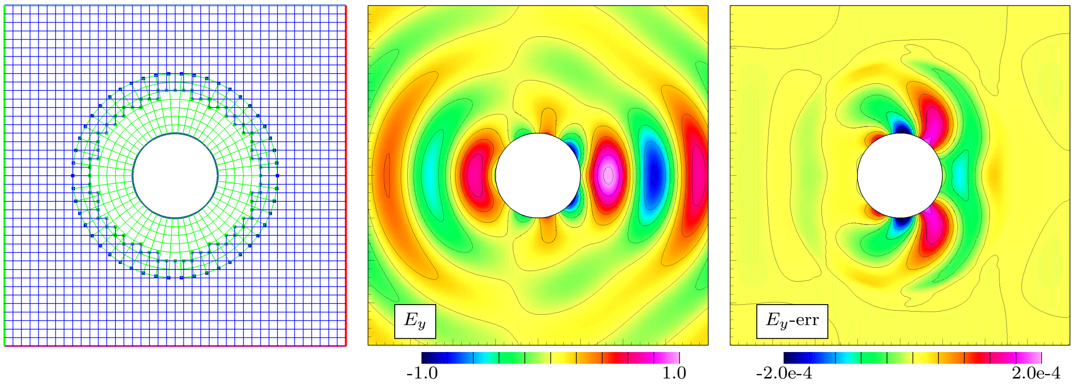

Figure 13: Scattering of a dispersive plane wave from a PEC cylinder. Solution at $t = 1.0$ using the fourth-order accurate ADE-GDM scheme and $C_{\rm cfl} = 0.9$. Left: coarse grid $\mathcal{G}^{(1)}$. Middle: E_y at $t = 1$ for $\mathcal{G}^{(4)}$. Right: error in E_y.

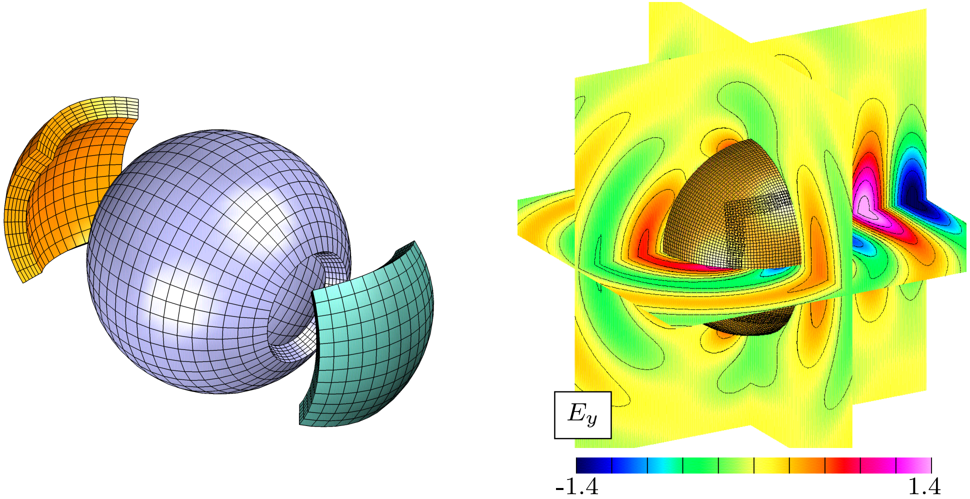

Figure 14: Left: component grids for the sphere. A spherical polar patch covers the main part of the sphere while orthographic patches cover the polar regions. The orthographic patches have been shifted outward for illustration purposes. At right is the computed scattered field E_y at $t = 0.5$ using $C_{\rm cfl} = 0.9$ on grid $\mathcal{G}^{(4)}$.

In the present work, the computational domain in two dimensions consists of the region exterior to a cylinder of radius $R = 0.5$ and interior to a surrounding square occupying the region $[-2, 2]^2$. The composite overlapping grid for this computational domain consists of a thin boundary-fitted annular grid, which cuts a hole in a Cartesian background grid. A coarse version of this composite grid is shown in Figure 13. The computational domain in three dimensions is taken to be the region inside the cube $[-2, 2]^3$ and exterior to a sphere of radius $R = 1$ centered at the origin. The composite overlapping grid for this geometry has one Cartesian background grid, and a series of grids to represent the boundary of the sphere. The grids near the sphere (see Figure 14) consist of three boundary-fitted patches, a spherical polar patch covering most of the sphere and two orthographic patches over the two polar regions, thus covering the polar singularities in the spherical polar patch. Additional details of the grids used here can be found in [7]. As before, we let $\mathcal{G}^{(j)}$ denote the grid with grid spacing approximately equal to $h_j = 1/(10j)$. The boundaries are taken as PEC boundary conditions on the cylinder (respectively, the sphere) while the exact solution is given on the far-field boundaries of the square. The incident field is a dispersive plane-wave propagating in the x-direction, and given by $\mathbf{E}^I = (0, e^{ikx-st}, 0)$. The wave number in all cases is taken as $k = 2\pi$, and s is determined from the dispersion relation (20) with $ck = 2\pi$ and GDM parameters $\mathcal{S}_{\rm ND}$ from Table 1.

GDM roots for the PEC cylinder and sphere	
ck	2π
s_R	$.9885130705264i$
s_N	$6.356198511198i$

Table 7: GDM roots of the dispersion relation corresponding to set $\mathcal{S}_{\rm ND}$ of GDM parameters shown in Table 1 for for scattering from a PEC cylinder or sphere.

The roots of the dispersion relation corresponding to resonant and non-resonant modes are shown in Table 7. The exact Mie series solution for the dispersive case is determined following

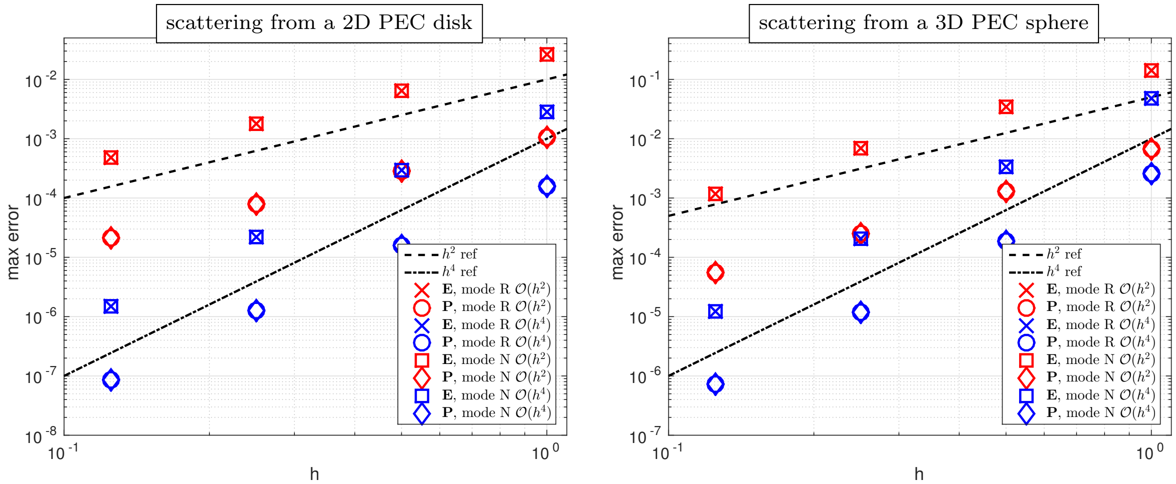

Figure 15: Convergence study in $\|\mathbf{E}\|_\infty$ and $\|\mathbf{P}\|_\infty$ for electromagnetic scattering from a perfect electrical cylinder (left), and a perfect electrical conducting sphere (right) using the second- and fourth-order schemes. All computations use the $\mathcal{S}_{\text{ND}}$ parameter set from Table 1, with corresponding resonant and non-resonant roots of the dispersion relation given in Table 7.

the process discussed in Section 6.1, and the computations determine the scattered field directly by subtracting out the incident plane wave. This adds right-hand side forcing terms to the PEC boundary conditions. In all cases the time step is chosen using $C_{\text{cfl}} = 0.9$.

Computations are performed for the $\mathcal{S}_{\text{ND}}$ parameter set, which yields a purely dispersive wave (i.e. the mode does not decay in time). This choice is made for physical reasons, since the problem is set up to correspond to a wave coming from the far field and interacting with a scatterer. In addition to a coarse version of the grid, Figure 13 shows the shaded contours of the computed E_y field as well as the error in E_y for the problem of scattering from a PEC cylinder. The computed solution from the fourth-order accurate scheme at $t = 1$, and the error reveals the smoothness of computed approximation and its error. Similarly, Figure 14 shows a coarse version of the composite grid used for scattering from a PEC sphere, as well as shaded contours of E_y at $t = 0.5$. More quantitative information about the performance of the second- and fourth-order schemes is given in Figure 15, which shows results of max-norm convergence studies for both the two- and three-dimensional cases. The observed convergence rates are in very good agreement with the expected rate for both second- and fourth-order schemes.

6.6. *GDM scattering from multiple bodies*

As a final example, we consider the scattering of a dispersive TE-z plane wave from a collection of embedded bodies with different shapes as shown in Figure 16. This case demonstrates the flexibility of the code to handle general complex geometries and provides an interesting comparison between an incident resonant and non-resonant mode. The exact solution is not known in this case and so computed solutions are compared on medium and fine resolution grids to illustrate grid convergence. The composite grid for the problem is shown in Figure 16. The grid, denoted by $\mathcal{G}_{\text{mb}}^{(j)}$ with target grid spacing $\Delta s_j = 1/(20j)$, covers the domain exterior to a collection of twelve bodies. A boundary fitted grid is formed around each of the bodies. These are enclosed in an inner background Cartesian grid of dimensions $[-3, 5.5] \times [-3.5, 3.5]$, which itself in enclosed in a larger and coarser Cartesian grid with dimensions $[-7, 9.5] \times [-7.5, 7.5]$ with double the grid spacing.

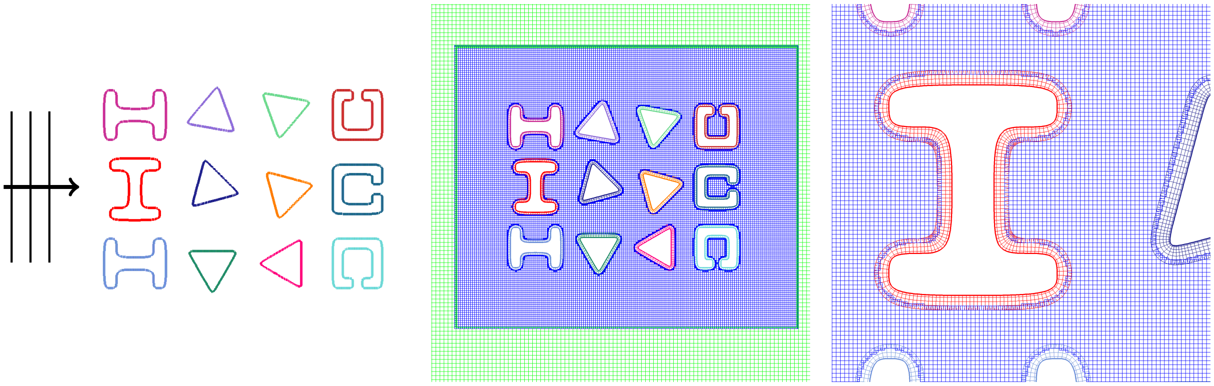

Figure 16: Left: configuration for scattering of a plane dispersive wave from a collection of bodies. Middle and right: the composite grid $\mathcal{G}_{\text{mb}}^{(4)}$ (coarsened for plotting purposes). A boundary fitted grid is generated near each body and enclosed within a background Cartesian grid (blue) of similar grid spacing which itself is enclosed in a larger background Cartesian grid (green) with double the grid spacing.

For this problem we take a dispersive material using parameter set $\mathcal{S}_{\text{ND}}$ from Table 2. The incident wave travels in the positive x-direction with $k_x = 4\pi$. The non-resonant mode has $s \approx -12.602356\, i$ and resonant mode has $s \approx -.99714456\, i$. The boundary conditions on the bodies are taken as perfect electrical conductors. The scattered field from an incident dispersive plane wave is computed directly, in the usual way, by subtracting the incident field and adjusting the PEC boundary conditions to be inhomogeneous. Far-field boundary conditions of Engquist-Majda type are applied on the outer boundary; these are designed for non-dispersive materials and thus are not as effective for the GDM material. Therefore the outer boundary is placed at a sufficient distance away so that any errors from the far-field do not affect the solution near the scatters for the times considered.

Figure 17 shows contours of the computed solution comparing a non-resonant and resonant mode. The solution is computed using the fourth-order accurate algorithm on grid $\mathcal{G}_{\text{mb}}^{(4)}$ and shown at times $t = 1$ and $t = 5$. The character of the resonant mode is clearly very different from the non-resonant mode. Due to the complex geometry, the reflected waves are a combination of many wave numbers and eigenmodes. The incident wave number $k = 4\pi$ is the same for both cases but the resonant mode has a much slower variation in time and it excites different modes of the system. To assess grid convergence, Figure 18 compares the computed solution at time $t = 5$ on grid $\mathcal{G}_{\text{mb}}^{(4)}$ with results for the finer grid $\mathcal{G}_{\text{mb}}^{(8)}$ using the fourth-order accurate scheme. The results are nearly indistinguishable.

7. Conclusions

Second-order and fourth-order accurate schemes have been developed for the solution of Maxwell's equations in second-order form with a generalized dispersion model (GDM). The dispersion model has been treated in the time domain by augmenting Maxwell's equations with a set of auxiliary differential equations (ADE) for a set of polarization vectors. An analysis of the dispersion relation for the ADE-GDM equations has been given, and the results of the analysis provides sufficient conditions on the coefficients in the GDM model to ensure that solutions do not grow in time. The numerical schemes are both three-level single-stage in time based on a Taylor time-stepping

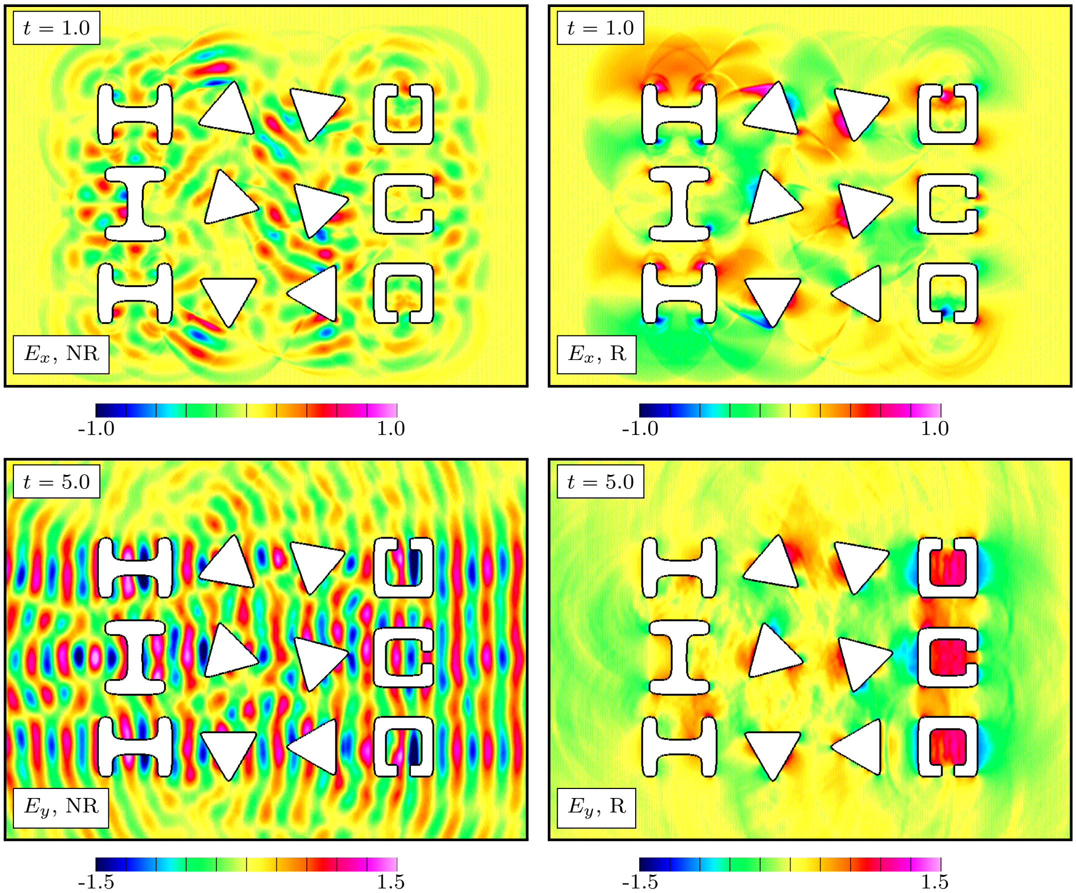

Figure 17: Non-resonant and resonant modes for scattering from a collection of PEC inclusions in a GDM material. The solutions on grid $\mathcal{G}_{\text{mb}}^{(4)}$ are compared at times $t = 1$ and $t = 5$. Results are from the fourth-order accurate scheme.

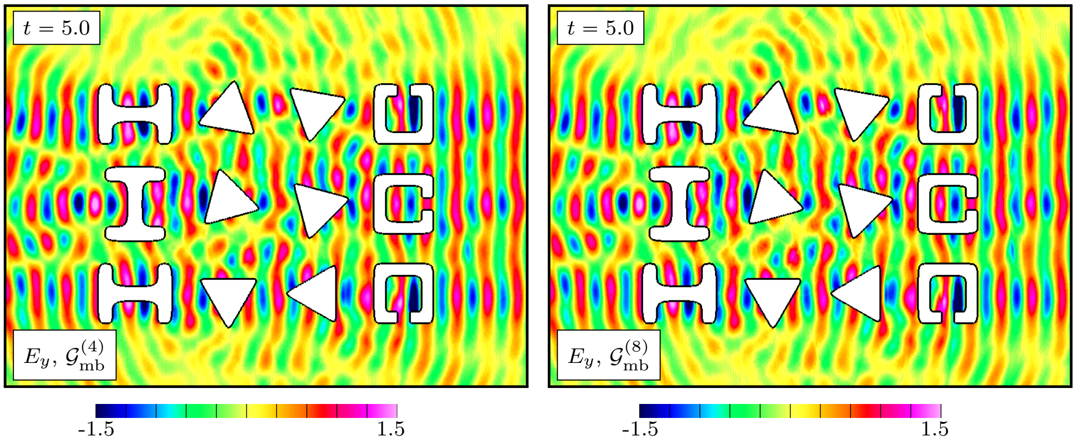

Figure 18: A comparison between solutions computed on grid $\mathcal{G}_{\text{mb}}^{(4)}$, and the finer grid $\mathcal{G}_{\text{mb}}^{(8)}$, for the non-resonant mode at time $t = 5$. Results are from the fourth-order accurate scheme. The two solutions are seen to be nearly indistinguishable.

approach. Finite-difference approximations are used in space, and composite overlapping grids are used to represent complex geometry. The stability of the schemes are analyzed with a von

Neumann analysis. The maximum stable time-step for both the second- and fourth-order accurate schemes are shown to be essentially the same "CFL-one" condition as for the non-dispersive case. Exact solutions to the ADE-GDM equations have been developed for eigenmodes of rectangular and cylindrical domains as well as for scattering from a PEC cylinder and sphere. Numerical results have been presented to confirm the accuracy and stability of the schemes for various geometries, where overlapping grids were used to deal with general curvilinear boundaries. High-order accurate treatment of interfaces between dispersive materials will be discussed in a future paper.

Appendix A. Properties of the GDM dispersion relation.

In this section we provide more details to the discussion in Section 2.2, regarding the conditions on the GDM parameters for which there are no roots of the dispersion relation with $\Re(s) > 0$, corresponding to growing modes in time. The dispersion relation (20) is simplified as a quartic of the form

$$f(s) = s^4 + Bs^3 + Cs^2 + Ds + E = 0, \tag{A.1}$$

where

$$\begin{aligned} B &= b_1 + a_1, \\ C &= (ck)^2 + b_0 + a_0, \\ D &= (ck)^2 b_1, \\ E &= (ck)^2 b_0. \end{aligned}$$

To determine if there are roots with positive $\Re(s)$ of the polynomial (A.1), we can use the argument principle from complex analysis to directly count the number of roots in the right-half plane[10] indicates that the number of roots N with $\Re(s) > 0$ satisfies the equation

$$2\pi i N = \oint_{\mathcal{C}} \frac{f'(s)}{f(s)}\, ds,$$

where the contour $\mathcal{C}$ encompasses the right half-plane. For simplicity, we take $\mathcal{C}$ to be the semi-circle $s = Re^{i\theta}$ for $\theta \in [-\pi/2, \pi/2]$ followed by the line $s = -iy$ for $y \in [-R, R]$, and subsequently take the limit $R \to \infty$. For the general polynomial (A.1) with real coefficients, this yields the equation

$$\begin{aligned} 2N = 4 &- \operatorname{sgn}(B)\left[1 - \operatorname{sgn}(B^2E - BCD + D^2)\right] \\ &- \operatorname{sgn}(BC - D)\left[1 - \operatorname{sgn}(B^2E - BCD + D^2)\operatorname{sgn}(E)\right]. \end{aligned}$$

---

[10] A method based on this principle [53] that has been recently used in a rapid eigen-decomposition scheme [54].

The necessary and sufficient conditions for all roots to have negative real parts are

$$B > 0, \tag{A.2}$$

$$E > 0, \tag{A.3}$$

$$BC - D > 0, \tag{A.4}$$

$$-B^2E + BCD - D^2 > 0. \tag{A.5}$$

In the present situation, we have assumed non-negative constants a_0, a_1 b_0, and b_1, which implies non-negative B and E. In addition, the condition (A.4) leads to the inequality

$$a_0a_1^2 + \left\{[b_0 + (ck)^2]a_1 + a_0b_1\right\} + b_0b_1 > 0,$$

which is clearly always satisfied since the parameters are all non-negative and so we have a sum of non-negative terms. Finally, the condition (A.5) leads to the inequality

$$(ck)^2\left[(a_1 + b_1)(a_0b_1 - a_1b_0) + a_1b_1(ck)^2\right] > 0,$$

which can clearly be violated if a_1b_0 is sufficiently large. Therefore, a practical sufficient, but not necessary, condition to avoid growing solutions is

$$a_0b_1 > a_1b_0. \tag{A.6}$$

Let us revisit this analysis using the Routh-Hurwitz theory [48]. We again investigate the general polynomial equation (2.2), for which the direct application of the Routh-Hurwitz theory yields the following necessary and sufficient conditions for all roots to have negative real parts

$$\begin{aligned} B &> 0, \\ E &> 0, \\ C - \frac{D}{B} &> 0, \\ D - \frac{BE}{C - \frac{D}{B}} &> 0. \end{aligned}$$

Using the first two conditions, the latter two conditions can be reduced, and the result is that the roots have negative real part if and only if

$$\begin{aligned} B &> 0, \\ E &> 0, \\ BC - D &> 0, \\ -D^2 + BCD - B^2E &> 0. \end{aligned}$$

This result is in agreement with the result derived previously via contour integration, but with these mechanics it is easier to derive conditions for the case of multiple polarization vectors. We have not found a simple condition on the GDM coefficients to ensure no growth for $N_p > 1$, but the Routh-Hurwitz conditions can always be checked numerically to determine if a given set of GDM coefficients leads to roots with $\Re(s) > 0$.

Appendix B. Fitting material properties using the GDM model

The Padé approximant is the *best* approximation to a given function (dielectric permittivity as a function of frequency in our case) by a rational function,

$$\hat{\epsilon}(s) = \frac{f_0 + f_1 s + f_2 s^2 + \ldots f_M s^M}{g_0 + g_1 s + g_2 s^2 + \ldots g_N s^N}, \tag{B.1}$$

and such approximations are often superior to polynomial approximations especially when the function has poles or near poles (that correspond to resonances or near resonances in the physical problem). Assuming real coefficients f_j and g_j with $M \leqslant N$, the rational function in (B.1) can be written as a sum of terms (partial fraction decomposition) involving simpler rational functions that takes the form of the GDM approximation

$$\hat{\epsilon}(s) = \epsilon_0 + \sum_{m=1}^{N_p} \frac{a_{0,m} + s\, a_{1,m}}{b_{0,m} + s\, b_{1,m} + s^2}. \tag{B.2}$$

The form (B.2) could be further reduced to a sum of terms with single poles, $\alpha_{0,m}/(\beta_{0,m}+s)$, but this would, in general, involve the introduction of complex coefficients for $\alpha_{0,m}$ and $\beta_{0,m}$ that we wish to avoid. The Debye, Drude, Lorentz, Sellmeier, and critical point (CP) models (or combinations thereof) are all special cases of the GDM model,

$$\hat{\epsilon}_{\text{Debye}}(s) = \frac{a_1}{b_1 + s}, \qquad \hat{\epsilon}_{\text{Drude}}(s) = \frac{a_0}{b_1 s + s^2}, \qquad \hat{\epsilon}_{\text{Lorentz}}(s) = \frac{a_0}{b_0 + b_1 s + s^2},$$
$$\hat{\epsilon}_{\text{Sellmeier}}(s) = \frac{a_0}{b_0 + s^2}, \qquad \hat{\epsilon}_{\text{Critical-Point}}(s) = \frac{\alpha}{s - \beta} + \frac{\bar{\alpha}}{s - \bar{\beta}} = \frac{a_0 + s\, a_1}{b_0 + s\, b_1 + s^2}, \qquad (\alpha, \beta \in \mathbb{C}).$$

Choosing the coefficients in the GDM approximation to fit experimentally or numerically obtained ellipsometry data is not a purely mathematical exercise. The fit should consider not only the mathematical approximation error, but also the desired frequency range of interest and the phys-

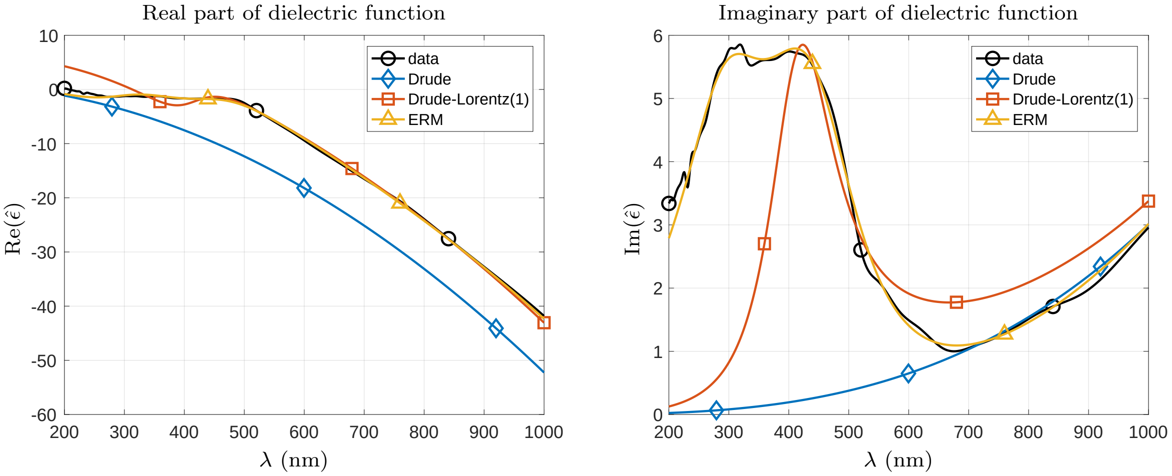

Figure B.19: A comparsion of different model fits for the dieletric permittivity of gold compared to experimental data [55]. The ERM model [56], which consists of one Drude and two critical-point terms is shown to provide a good approximation over the wavelengths considered.

ical properties of the material,[11] see [56], for example. Unfortunately, the purely mathematical approach, where one simply fits the permittivity data with enough terms to get a prescribed error, but without accounting for the physics, is potentially fraught with problems. The terms in such a mathematical fit may, for example, introduce combinations of gain terms in a physically lossy material. This situation may lead to numerical solutions that can grow in time when physically they should decay, not to mention an unnecessary increase in computational costs. This explains why it is important to know the mathematical properties of the GDM model so that constraints can be placed on the coefficients to, for example, preclude growth in time when there should be none; the constraints derived in Appendix A can be used for this purpose.

Experimental data for the permittivity of various materials along with theoretical fits can be conveniently viewed and downloaded using the PhontonicsDB tool [57] on the nanoHUB [58]. Figure B.19, for example, show fits of the permittivity $\hat{\epsilon}$ for gold, as a function of wavelength, compared to experimental data from Johnson and Christy [55]. Shown are the results for a Drude, Drude plus one Lorentz term, and the ERM model [56] which consists of one Drude and two critical-point terms. The ERM model provides a reasonably good approximation over the wavelengths considered. We also note that the GDM model has been used to directly fit theoretical models for the dielectric function of graphene [59]. The theoretical models involve principal value integrals that would be very difficult to treat directly in the time domain.

Appendix C. Algorithms for the second- and fourth-order accurate ADE-GDM schemes

In the following sections, we provide details of our efficient implementations of the second- and fourth-order accurate schemes outlined in Sections 3.1 and 3.2, respectively. These algorithms employ decoupled solutions of the linear operators in (28), (34) and (41) so that the updates of the components of electric field and N_p polarization vectors are performed explicitly.

Appendix C.1. Algorithm for the second-order accurate ADE-GDM scheme

The implementation of the second-order accurate ADE-GDM scheme given in Section 3.1 is provided in Algorithm 1.

The solutions for $\mathbf{E}^0_{\mathbf{j}}$ and $\mathbf{P}^0_{m,\mathbf{j}}$ at the start, $n = 0$, are determined from the initial conditions, while the solutions at the first time step, $n = 1$, (lines 3 and 6) are evaluated using a Taylor series in time. In the time-stepping loop (lines 10–20), the second-order accurate explicit updates for $\mathbf{E}^{n+1}_{\mathbf{j}}$ and $\mathbf{P}^{n+1}_{m,\mathbf{j}}$ are determined in lines 15 and 17, respectively. To obtain the formulas for these updates, we note that (23b) can be solved for $\mathbf{P}^{n+1}_{m,\mathbf{j}}$ in terms of $\mathbf{E}^{n+1}_{\mathbf{j}}$ and a remainder,

$$\mathbf{P}^{n+1}_{m,\mathbf{j}} = \frac{\Delta t}{2}\, \breve{a}_{1,m}\, \beta_m\, \mathbf{E}^{n+1}_{\mathbf{j}} + \beta_m\, \mathbf{R}_m, \tag{C.1}$$

where β_m and $\mathbf{R}_m$ are defined on lines 7 and 12, respectively. Equation (C.1) can be summed over m to determine $\mathbf{P}^{n+1}_{\mathbf{j}}$ in terms of $\mathbf{E}^{n+1}_{\mathbf{j}}$ and another remainder. This equation for $\mathbf{P}^{n+1}_{\mathbf{j}}$ is substituted into (23a) and subsequently solved for $\mathbf{E}^{n+1}_{\mathbf{j}}$ (line 15). Given $\mathbf{E}^{n+1}_{\mathbf{j}}$, the values of $\mathbf{P}^{n+1}_{m,\mathbf{j}}$ are found from (C.1) (line 17).

---

[11] It is known, for example, that gold has at least two interband transitions in the violet/near-ultra-violet region that should generally be included in the dielectric model.

Algorithm 1 Second-order accurate ADE-GDM algorithm.

```
1: $t = 0, n = 0;$
2: $\mathbf{E}^0_{\mathbf{j}} = \mathbf{E}^0(\mathbf{x}_{\mathbf{j}});$    ▷ Initialize $\mathbf{E}^0_{\mathbf{j}}$ using $\mathbf{E}(\mathbf{x}_{\mathbf{j}}, 0) = \mathbf{E}^0(\mathbf{x}_{\mathbf{j}})$
3: $\mathbf{E}^1_{\mathbf{j}} = \mathbf{E}^0(\mathbf{x}_{\mathbf{j}}) + \mathbf{E}^1(\mathbf{x}_{\mathbf{j}})\Delta t;$    ▷ Initialize $\mathbf{E}^1_{\mathbf{j}}$ using $\mathbf{E}(\mathbf{x}_{\mathbf{j}}, 0) = \mathbf{E}^0(\mathbf{x}_{\mathbf{j}})$, $\partial_t \mathbf{E}(\mathbf{x}_{\mathbf{j}}, 0) = \mathbf{E}^1(\mathbf{x}_{\mathbf{j}})$
4: for $m = 1, \dots, N_p$ do
5:     $\mathbf{P}^0_{m,\mathbf{j}} = \mathbf{P}^0_m(\mathbf{x}_{\mathbf{j}});$    ▷ Initialize $\mathbf{P}^0_{m,\mathbf{j}}$ using $\mathbf{P}_m(\mathbf{x}_{\mathbf{j}}, 0) = \mathbf{P}^0_m(\mathbf{x}_{\mathbf{j}})$
6:     $\mathbf{P}^1_{m,\mathbf{j}} = \mathbf{P}^0_m(\mathbf{x}_{\mathbf{j}}) + \mathbf{P}^1_m(\mathbf{x}_{\mathbf{j}})\Delta t;$    ▷ Initialize $\mathbf{P}^1_{m,\mathbf{j}}$ using $\mathbf{P}_m(\mathbf{x}_{\mathbf{j}}, 0) = \mathbf{P}^0_m(\mathbf{x}_{\mathbf{j}})$, $\partial_t \mathbf{P}_m \mathbf{x}_{\mathbf{j}}, 0) = \mathbf{P}^1_m(\mathbf{x}_{\mathbf{j}})$
7:     $\beta_m = (1 + \frac{\Delta t}{2} b_{1,m})^{-1};$
8: end for
9: $\beta = \frac{\Delta t}{2} \sum_m \check{a}_{1,m} \beta_m;$
10: while $t < t_{final}$ do
11:     for $m = 1, \dots, N_p$ do
12:         $\mathbf{R}_m = 2\mathbf{P}^n_{m,\mathbf{j}} - \mathbf{P}^{n-1}_{m,\mathbf{j}} + \frac{\Delta t}{2} b_{1,m} \mathbf{P}^{n-1}_{m,\mathbf{j}} - \Delta t^2 b_{0,m} \mathbf{P}^n_{m,\mathbf{j}} + \Delta t^2 \check{a}_{0,m} \mathbf{E}^n_{\mathbf{j}} - \frac{\Delta t}{2} \check{a}_{1,m} \mathbf{E}^{n-1}_{\mathbf{j}};$
13:     end for
14:     $\mathbf{R} = \sum_m \beta_m \mathbf{R}_m;$
15:     $\mathbf{E}^{n+1}_{\mathbf{j}} = (1 + \epsilon_0^{-1}\beta)^{-1}\Big[2\mathbf{E}^n_{\mathbf{j}} - \mathbf{E}^{n-1}_{\mathbf{j}} + \Delta t^2 c^2 \Delta_{2h} \mathbf{E}^n_{\mathbf{j}} + \epsilon_0^{-1} \sum_m \Big\{2\mathbf{P}^n_{m,\mathbf{j}} - \mathbf{P}^{n-1}_{m,\mathbf{j}}\Big\} - \epsilon_0^{-1} \mathbf{R}\Big];$
16:     for $m = 1, \dots, N_p$ do
17:         $\mathbf{P}^{n+1}_{m,\mathbf{j}} = \frac{\Delta t}{2} \check{a}_{1,m} \beta_m \mathbf{E}^{n+1}_{\mathbf{j}} + \beta_m \mathbf{R}_m;$    ▷ (C.1)
18:     end for
19:     $t = t + \Delta t,\ n = n + 1;$
20: end while
```

Appendix C.2. Algorithm for the fourth-order accurate ADE-GDM scheme

The implementation of the fourth-order accurate ADE-GDM scheme given in Section 3.2 is provided in Algorithm 2.

The numerical solution values at first time-step, $n = 1$, (lines 3 and 6), are determined using a Taylor series in time. These series use higher time-derivatives of the initial conditions that can be derived by using the governing partial differential equations to replace time derivatives in terms of known spatial derivatives at $t = 0$. For example, the second time-derivative of $\mathbf{P}_m$ can be evaluated at $t = 0$ using

$$\mathbf{P}_{m,tt}(\mathbf{x}_{\mathbf{j}}, 0) \overset{\text{def}}{=} a_{1,m}\mathbf{E}^1(\mathbf{x}_{\mathbf{j}}) + a_{0,m}\mathbf{E}^0(\mathbf{x}_{\mathbf{j}}) - b_{1,m}\mathbf{P}^1_m(\mathbf{x}_{\mathbf{j}}) - b_{0,m}\mathbf{P}^0_m(\mathbf{x}_{\mathbf{j}}).$$

In the time-stepping loop (lines 8–36), temporary second-order accurate updates are computed first in lines 10–23 (see Appendix C.1), which are then used to compute derived quantities, such as $\big[\partial_t \mathbf{P}^*_m\big]^n_{\mathbf{j}}$ (line 19). The fourth-order accurate explicit updates for $\mathbf{E}^{n+1}_{\mathbf{j}}$ and $\mathbf{P}^{n+1}_{m,\mathbf{j}}$ are then performed in lines 31 and 33, respectively, using formulas obtained from (32) and (35) in an analogous fashion to the second-order updates. In particular, (35) can be solved for $\mathbf{P}^{n+1}_{m,\mathbf{j}}$ in terms of $\mathbf{E}^{n+1}_{\mathbf{j}}$ and a remainder,

$$\mathbf{P}^{n+1}_{m,\mathbf{j}} = \frac{1}{\gamma_m}\left[\left(a_{1,m}\frac{\Delta t}{2} + a_{0,m}\frac{\Delta t^2}{12}\right)\mathbf{E}^{n+1}_{\mathbf{j}} + \mathbf{R}_m\right], \tag{C.2}$$

where γ_m and $\mathbf{R}_m$ are given in lines 26 and 27, respectively. Summing (C.2) over m leads to an equation for $\mathbf{P}^{n+1}_{\mathbf{j}}$ in terms of $\mathbf{E}^{n+1}_{\mathbf{j}}$, and then substituting this equation into (32) and solving for $\mathbf{E}^{n+1}_{\mathbf{j}}$ leads to the update on line 31. Given $\mathbf{E}^{n+1}_{\mathbf{j}}$, the values for $\mathbf{P}^{n+1}_{m,\mathbf{j}}$ can then be evaluated from (C.2) which gives the update on line 33.

Algorithm 2 Fourth-order accurate ADE-GDM algorithm.

```
$t = 0, n = 0$;
for $m = 1, \dots, N_p$ do
    $\mathbf{P}^0_{m,\mathbf{j}} = \mathbf{P}^0_m(\mathbf{x}_\mathbf{j})$;   $\mathbf{P}^1_{m,\mathbf{j}} = \mathbf{P}^0_m(\mathbf{x}_\mathbf{j}) + \mathbf{P}^1_m(\mathbf{x}_\mathbf{j})\Delta t + \mathbf{P}_{m,tt}(\mathbf{x}_\mathbf{j},0)\frac{\Delta t^2}{2} + \mathbf{P}_{m,ttt}(\mathbf{x}_\mathbf{j},0)\frac{\Delta t^3}{6}$; ▷ Init. $\mathbf{P}^0_{m,\mathbf{j}}$ and $\mathbf{P}^1_{m,\mathbf{j}}$
    $\beta_m = (1 + \frac{\Delta t}{2}\, b_{1,m})^{-1}$;
end for
$\mathbf{E}^0_\mathbf{j} = \mathbf{E}^0(\mathbf{x}_\mathbf{j})$;   $\mathbf{E}^1_\mathbf{j} = \mathbf{E}^0(\mathbf{x}_\mathbf{j}) + \mathbf{E}^1(\mathbf{x}_\mathbf{j})\Delta t + \mathbf{E}_{tt}(\mathbf{x}_\mathbf{j},0)\frac{\Delta t^2}{2} + \mathbf{E}_{ttt}(\mathbf{x}_\mathbf{j},0)\frac{\Delta t^3}{6}$;   ▷ Init. $\mathbf{E}^0_\mathbf{j}$ and $\mathbf{E}^1_\mathbf{j}$
$\beta = (\Delta t/2)\sum_m \breve{a}_{1,m}\,\beta_m$;
while $t < t_{final}$ do
    // Evaluate second-order accurate predictions $\mathbf{E}^{*\,n+1}_{\mathbf{j}}$ and $\mathbf{P}^{*\,n+1}_{m,\mathbf{j}}$
    for $m = 1, \dots, N_p$ do
        $\mathbf{R}_m = 2\mathbf{P}^n_{m,\mathbf{j}} - \mathbf{P}^{n-1}_{m,\mathbf{j}} + \frac{\Delta t}{2}\, b_{1,m}\mathbf{P}^{n-1}_{m,\mathbf{j}} - \Delta t^2\, b_{0,m}\mathbf{P}^n_{m,\mathbf{j}} + \Delta t^2\, \breve{a}_{0,m}\mathbf{E}^n_\mathbf{j} - \frac{\Delta t}{2}\, \breve{a}_{1,m}\mathbf{E}^{n-1}_\mathbf{j}$;
    end for
    $\mathbf{R} = \sum_m \beta_m \mathbf{R}_m$;   ▷ Full right-hand side for polarization prediction $\mathbf{P}^{*\,n+1}$
    $\mathbf{E}^{*\,n+1}_{\mathbf{j}} = (1 + \epsilon_0^{-1}\beta)^{-1}\Big[2\mathbf{E}^n_\mathbf{j} - \mathbf{E}^{n-1}_\mathbf{j} + \Delta t^2 c^2 \Delta_{2h}\mathbf{E}^n_\mathbf{j} + \epsilon_0^{-1}\sum_m \Big\{2\mathbf{P}^n_{m,\mathbf{j}} - \mathbf{P}^{n-1}_{m,\mathbf{j}}\Big\} - \epsilon_0^{-1}\,\mathbf{R}\Big]$;
    $\big[\partial_t \mathbf{E}^*\big]^n_\mathbf{j} = (\mathbf{E}^{*\,n+1}_{\mathbf{j}} - \mathbf{E}^{n-1}_\mathbf{j})/(2\Delta t)$;   $\big[\partial_t^2 \mathbf{E}^*\big]^n_\mathbf{j} = (\mathbf{E}^{*\,n+1}_{\mathbf{j}} - 2\mathbf{E}^n_\mathbf{j} + \mathbf{E}^{n-1}_\mathbf{j})/\Delta t^2$;
    $\big[\Delta_{2h}\partial_t \mathbf{E}^*\big]^n_\mathbf{j} = \Delta_{2h}(\mathbf{E}^{*\,n+1}_{\mathbf{j}} - \mathbf{E}^{n-1}_\mathbf{j})/(2\Delta t)$;
    for $m = 1, \dots, N_p$ do
        $\mathbf{P}^{*\,n+1}_{m,\mathbf{j}} = \frac{\Delta t}{2}\, \breve{a}_{1,m}\,\beta_m\, \mathbf{E}^{*\,n+1}_{\mathbf{j}} + \beta_m\, \mathbf{R}_m$;   ▷ Second-order accurate prediction (C.1) for $\mathbf{P}^{*\,n+1}_{m,\mathbf{j}}$
        $\big[\partial_t \mathbf{P}^*_m\big]^n_\mathbf{j} = (\mathbf{P}^{*\,n+1}_{m,\mathbf{j}} - \mathbf{P}^{n-1}_{m,\mathbf{j}})/(2\Delta t)$;
        $\big[\partial_t^3 \mathbf{P}^*_m\big]^n_\mathbf{j} = b^{(3)}_{1,m}\big[\partial_t \mathbf{P}^*_m\big]^n_\mathbf{j} + b^{(3)}_{0,m}\mathbf{P}_{m,\mathbf{j}} + \breve{a}^{(3)}_{0,m}\mathbf{E}_\mathbf{j} + \breve{a}^{(3)}_{1,m}\big[\partial_t \mathbf{E}^*\big]^n_\mathbf{j} + \breve{a}^{(3)}_{2,m}\big[\partial_t^2 \mathbf{E}^*\big]^n_\mathbf{j}$;
    end for
    $\mathbf{P}^{*\,n+1}_{\mathbf{j}} = \sum_m \mathbf{P}^{*\,n+1}_{m,\mathbf{j}}$;
    $\big[\Delta_{2h}\partial_t^2 \mathbf{P}^*\big]^n_\mathbf{j} = \Delta_{2h}(\mathbf{P}^{*\,n+1}_{\mathbf{j}} - 2\mathbf{P}^n_\mathbf{j} + \mathbf{P}^{n-1}_\mathbf{j})/\Delta t^2$;   $\big[\partial_t^3 \mathbf{E}^*\big]^n_\mathbf{j} = c^2\big[\Delta_{2h}\partial_t \mathbf{E}^*\big]^n_\mathbf{j} - \epsilon_0^{-1}\big[\partial_t^3 \mathbf{P}^*\big]^n_\mathbf{j}$;
    // Evaluate fourth-order accurate updates.
    for $m = 1, \dots, N_p$ do
        $\gamma_m = 1 + b_{1,m}\frac{\Delta t}{2} + b_{0,m}\frac{\Delta t^2}{12}$;
        $\mathbf{R}_m = \Big(1 + b_{1,m}\frac{\Delta t^2}{12}\Big)\Big(2\mathbf{P}^n_{m,\mathbf{j}} - \mathbf{P}^{n-1}_{m,\mathbf{j}}\Big) + \frac{\Delta t}{2}\, b_{1,m}\mathbf{P}^{n-1}_{m,\mathbf{j}} - \Delta t^2\, b_{0,m}\mathbf{P}^n_{m,\mathbf{j}} + \Delta t^2\, \breve{a}_{0,m}\mathbf{E}^n_\mathbf{j}$
                $-\frac{\Delta t}{2}\, \breve{a}_{1,m}\mathbf{E}^{n-1}_\mathbf{j} - \breve{a}_{0,m}\frac{\Delta t^2}{12}\Big(2\mathbf{E}^n_\mathbf{j} - \mathbf{E}^{n-1}_\mathbf{j}\Big) + b_{1,m}\frac{\Delta t^2}{12}\big[\partial_t^3 \mathbf{P}^*_m\big]^n_\mathbf{j} - \breve{a}_{1,m}\frac{\Delta t^2}{12}\big[\partial_t^3 \mathbf{E}^*\big]^n_\mathbf{j}$;
    end for
    $\gamma_E = \sum_m \Big(-a_{1,m}\frac{\Delta t}{2} - a_{0,m}\frac{\Delta t^2}{12}\Big)/\gamma_m$;   $\mathbf{R}_P = \sum_m \mathbf{R}_m/\gamma_m$;
    $\mathbf{R}_E = 2\mathbf{E}^n_\mathbf{j} - \mathbf{E}^{n-1}_\mathbf{j} + \Delta t^2 c^2 \Delta_{2h}\mathbf{E}^n_\mathbf{j} + \epsilon_0^{-1}\sum_m \Big\{2\mathbf{P}^n_{m,\mathbf{j}} - \mathbf{P}^{n-1}_{m,\mathbf{j}}\Big\} + \frac{\Delta t^2}{12}\Big((c^2\Delta_{2h})^2\mathbf{E}^n_\mathbf{j} - \epsilon_0^{-1}c^2\big[\Delta_{2h}\partial_t^2 \mathbf{P}^*\big]^n_\mathbf{j}\Big)$
    $\mathbf{E}^{n+1}_\mathbf{j} = (\gamma_E\mathbf{R}_P - \mathbf{R}_E)/(\epsilon_0^{-1}\gamma_E - 1)$ ;
    for $m = 1, \dots, N_p$ do
        $\mathbf{P}^{n+1}_{m,\mathbf{j}} = \gamma_m^{-1}\mathbf{R}_m + \gamma_m^{-1}\Big(a_{1,m}\frac{\Delta t}{2} + a_{0,m}\frac{\Delta t^2}{12}\Big)\mathbf{E}^{n+1}_\mathbf{j}$;
    end for
    $t = t + \Delta t$, $n = n + 1$;
end while
```

References

[1] J. S. Hesthaven, High-order accurate methods in time-domain computational electromagnetics: A review, Advances in imaging and electron physics 127 (2003) 59–123.

[2] A. Taflove, S. C. Hagness, Computational Electrodynamics: The Finite-Difference Time-Domain Method, Artech House, 2000.

[3] G. C. Cohen, Higher-Order Numerical Methods for Transient Wave Equations, Springer, New York, 2002.

[4] K. S. Yee, Numerical solution of initial boundary value problems involving Maxwell's equations in isotropic media, IEEE Transactions on Antennas and Propogation 14 (1966) 302–307.

[5] J. Nédélec, Mixed finite elements in $\mathcal{R}^3$, Numer. Math. 35 (1980) 315–341.

[6] W. D. Henshaw, A high-order accurate parallel solver for Maxwell's equations on overlapping grids, SIAM J. Sci. Comput. 28 (2006) 1730–1765.

[7] J. Angel, J. W. Banks, W. D. Henshaw, High-order upwind schemes for the wave equation on overlapping grids: Maxwell's equations in second-order form, J. Comput. Phys. 352 (2018) 534–567.

[8] J. W. Banks, W. D. Henshaw, Upwind schemes for the wave equation in second-order form, J. Comput. Phys. 231 (2012) 5854–5889.

[9] K. S. Cole, R. H. Cole, Dispersion and absorption in dielectrics I. Alternating current characteristics, The Journal of Chemical Physics 9 (1941) 341–351.

[10] D. W. Davidson, R. H. Cole, Dielectric relaxation in glycerol, propylene glycol, and npropanol, The Journal of Chemical Physics 19 (1951) 1484–1490.

[11] S. Havriliak, S. Negami, A complex plane analysis of α-dispersions in some polymer systems, Journal of Polymer Science Part C: Polymer Symposia 14 (1951) 99–117.

[12] S. Havriliak, S. Negami, A complex plane representation of dielectric and mechanical relaxation processes in some polymers, Polymer 8 (1967) 161 – 210.

[13] S. Gabriel, R. W. Lau, C. Gabriel, The dielectric properties of biological tissues: III. Parametric models for the dielectric spectrum of tissues, Physics in Medicine & Biology 41 (1996) 2271.

[14] A. Robert, Dielectric permittivity of concrete between 50 mhz and 1 Ghz and GPR measurements for building materials evaluation, Journal of Applied Geophysics 40 (1998) 89 – 94.

[15] F. Torres, P. Vaudon, B. Jecko, Application of fractional derivatives to the FDTD modeling of pulse propagation in a Cole-Cole dispersive medium, Microwave and Optical Technology Letters 13 (1996) 300–304.

[16] L. Mescia, P. Bia, D. Caratelli, Fractional derivative based FDTD modeling of transient wave propagation in Havriliak-Negami media, IEEE Transactions on Microwave Theory and Techniques 62 (2014) 1920–1929.

[17] I. T. Rekanos, T. V. Yioultsis, Approximation of Grünwald-Letnikov fractional derivative for FDTD modeling of Cole-Cole media, IEEE Transactions on Magnetics 50 (2014) 181–184.

[18] L. J. Prokopeva, J. D. Borneman, A. V. Kildishev, Optical dispersion models for time-domain modeling of metal-dielectric nanostructures, IEEE Transactions on Magnetics 47 (2011) 1150–1153.

[19] R. Luebbers, F. P. Hunsberger, K. S. Kunz, R. B. Standler, M. Schneider, A frequency-dependent finite-difference time-domain formulation for dispersive materials, IEEE Transactions on Electromagnetic Compatibility 32 (1990) 222–227.

[20] R. J. Luebbers, F. Hunsberger, K. S. Kunz, A frequency-dependent finite-difference time-domain formulation for transient propagation in plasma, IEEE Transactions on Antennas and Propagation 39 (1991) 29–34.

[21] R. J. Luebbers, F. Hunsberger, FDTD for Nth-order dispersive media, IEEE Transactions on Antennas and Propagation 40 (1992) 1297–1301.

[22] D. Kelley, R. Luebbers, Piecewise linear recursive convolution for dispersive media using FDTD, IEEE Transactions on Antennas and Propagation 44 (1996) 792–797.

[23] K. Chun, H. Kim, H. Kim, Y. Chung, PLRC and ADE implementations of Drude-critical point dispersive model for the FDTD method, Progress in Electromagnetics Research 135 (2013) 373–390.

[24] T. Kashiwa, N. Yoshida, I. Fukai, A treatment by the finite-difference time-domain method of the dispersive characteristics associated with orientation polarization, IEICE Transactions E73 (1990) 1326–1328.

[25] T. Kashiwa, I. Fukai, A treatment by the FD-TD method of the dispersive characteristics associated with electronic polarization, Microwave and Optical Technology Letters 3 (1990) 203–205.

[26] T. Kashiwa, Y. Ohtomo, I. Fukai, A finite-difference time-domain formulation for transient propagation in dispersive media associated with Cole-Cole's circular arc law, Microwave and Optical Technology Letters 3 (1990) 416–419.

[27] R. M. Joseph, S. C. Hagness, A. Taflove, Direct time integration of Maxwell's equations in linear dispersive media with absorption for scattering and propagation of femtosecond electromagnetic pulses, Optics Letters 16 (1991) 1412–1414.

[28] O. P. Gandhi, B.-Q. Gao, J.-Y. Chen, A frequency-dependent finite-difference time-domain formulation for general dispersive media, IEEE Transactions on Microwave Theory and Techniques 41 (1993) 658–665.

[29] J. L. Young, A. Kittichartphayak, Y. M. Kwok, D. Sullivan, On the dispersion errors related to $(\mathrm{FD})^2\mathrm{TD}$ type schemes, IEEE transactions on microwave theory and techniques 43 (1995) 1902–1910.

[30] J. L. Young, A higher order FDTD method for EM propagation in a collisionless cold plasma, IEEE Transactions on Antennas and Propagation 44 (1996) 1283–1289.

[31] J. L. Young, D. Gaitonde, J. Shang, Toward the construction of a fourth-order difference scheme for transient EM wave simulation: Staggered grid approach, IEEE Transactions on Antennas and Propagation 45 (1997) 1573–1580.

[32] K. Prokopidis, E. Kosmidou, T. Tsiboukis, An FDTD algorithm for wave propagation in dispersive media using higher-order schemes, Journal of Electromagnetic Waves and Applications 18 (2004) 1171–1194.

[33] K. Prokopidis, T. Tsiboukis, Higher-order spatial FDTD schemes for EM propagation in dispersive media, in: Electromagnetic fields in mechatronics, electrical and electronic engineering: proceedings of ISEF'05, Vol. 27, Studies in Applied Electromagnetics and Mechanics, 2006, pp. 240–246.

[34] M. Jenkinson, J. Banks, High-order accurate FDTD schemes for dispersive Maxwell's equations in second-order form using recursive convolutions, Journal of Computational and Applied Mathematics 336 (2018) 192 – 218.

[35] L. J. Prokopeva, J. Trieschmann, T. A. Klar, A. V. Kildishev, Numerical modeling of active plasmonic metamaterials, Proc. of SPIE 8172 (2011) 81720.

[36] T. Lu, P. Zhang, W. Cai, Discontinuous Galerkin methods for dispersive and lossy Maxwell's equations and PML boundary conditions, Journal of Computational Physics 200 (2004) 549 – 580.

[37] S. D. Gedney, J. C. Young, T. C. Kramer, J. A. Roden, A discontinuous Galerkin finite element time-domain method modeling of dispersive media, IEEE Transactions on Antennas and Propagation 60 (2012) 1969–1977.

[38] D. Jiao, J.-M. Jin, Time-domain finite-element modeling of dispersive media, IEEE Microwave and Wireless Components Letters 11 (2001) 220–222.

[39] J. Li, Error analysis of finite element methods for 3-D Maxwell's equations in dispersive media, J. Comput. Appl. Math. 188 (2006) 107–120.

[40] H. Banks, V. Bokil, N. Gibson, Analysis of stability and dispersion in a finite element method for Debye and Lorentz dispersive media, Numerical Methods for Partial Differential Equations 25 (2009) 885–917.

[41] J. Sipe, V. So, M. Fukui, G. Stegeman, Analysis of second-harmonic generation at metal surfaces, Phys. Rev. B 21 (1980) 4389–4402.

[42] Y. Zeng, W. Hoyer, J. Liu, S. W. Koch, J. V. Moloney, Classical theory for second-harmonic generation from metallic nanoparticles, Phys. Rev. B 79 (2009) 235109.

[43] J. Liu, M. Brio, Y. Zeng, A. R. Zakharian, W. Hoyer, S. W. Koch, J. V. Moloney, Generalization of the FDTD algorithm for simulations of hydrodynamic nonlinear Drude model, Journal of Computational Physics 229 (2010) 5921 – 5932.

[44] M. Scalora, M. Vincenti, D. de Ceglia, V. Roppo, M. Centini, N. Akozbek, M. Bloemer, Second- and third- harmonic generation in metal-based structures, Phys. Rev. A 82 (2010) 043828.

[45] C. Ciraci, J. B. Pendry, D. R. Smith, Hydrodynamic model for plasmonics: A macroscopic approach to a microscopic problem, ChemPhysChem 14 (2013) 1109–1116.

[46] P. Ginzburg, A. V. Krasavin, G. A. Wurtz, A. V. Zayats, Nonperturbative hydrodynamic model for multiple harmonics generation in metallic nanostructures, ACS Photonics 2 (2015) 8–13.

[47] F. Vidal-Codina, N. Nguyen, S.-H. Oh, J. Peraire, A hybridizable discontinuous Galerkin method for computing nonlocal electromagnetic effects in three-dimensional metallic nanostructures, Journal of Computational Physics 355 (2018) 548 – 565.

[48] F. Gantmacher, J. Brenner, Applications of the Theory of Matrices, Dover Books on Mathematics, Dover Publications, 2005.

[49] W. D. Henshaw, Ogen: An overlapping grid generator for Overture, Research Report UCRL-MA-132237, Lawrence Livermore National Laboratory (1998).

[50] G. S. Chesshire, W. D. Henshaw, Composite overlapping meshes for the solution of partial differential equations, J. Comput. Phys. 90 (1990) 1–64.

[51] D. Appelö, J. W. Banks, W. D. Henshaw, D. W. Schwendeman, Numerical methods for solid mechanics on overlapping grids: Linear elasticity, J. Comput. Phys. 231 (2012) 6012–6050.

[52] J. Angel, J. W. Banks, W. D. Henshaw, Efficient high-order upwind difference schemes for the second-order wave equation on overlapping grids, Tech. rep., in preparation (2018).

[53] T. Sakurai, H. Sugiura, A projection method for generalized eigenvalue problems using numerical integration, Journal of Computational and Applied Mathematics 159 (2003) 119 – 128.

[54] A. O. Korotkevich, X. Ni, A. V. Kildishev, Fast eigensolver for plasmonic metasurfaces, Opt. Mater. Express 4 (2014) 288–299.

[55] P. B. Johnson, R. W. Christy, Optical constants of the noble metals, Phys. Rev. B 6 (1972) 4370–4379.

[56] P. Etchegoin, E. L. Ru, M. Meyer, An analytic model for the optical properties of gold, The Journal of Cehmical Physics 125.

[57] X. Ni, Z. Liu, A. V. Kildishev, PhotonicsDB: Optical constants, `https://nanohub.org/-resources/photonicsdb` (Feb 2008).

[58] Nanohub web page, nanoHUB.org.

[59] L. J. Prokopeva, A. V. Kildishev, Efficient time-domain model of the graphene dielectric function, in: Metamaterials: Fundamentals and Applications VI, Vol. 8806, Proceedings of the SPIE, 2013.